Process Modeling and Optimization of Powder Bed Additive Manufacturing of Inconel

Material

by

Faiyaz Ahsan

A Dissertation Presented in Partial Fulfillment
of the Requirements for the Degree
Doctor of Philosophy

Approved October 2021 by the
Graduate Supervisory Committee:

Leila Ladani, Chair
Jafar Razmi
Beomjin Kwon
Qiong Nian
Houlong Zhuang

ARIZONA STATE UNIVERSITY

December 2021

ABSTRACT

Laser powder bed fusion (LPBF) additive manufacturing (AM) has received

widespread attention due to its ability to produce parts with complicated design and better

surface finish compared to other additive techniques. LPBF uses a laser heat source to

melt layers of powder particles and manufactures a part based on the CAD design. This

process can benefit significantly through computational modeling. The objective of this

thesis was to understand the thermal transport, and fluid flow phenomena of the process,

and to optimize the main process parameters such as laser power and scan speed through

a combination of computational, experimental, and statistical analysis. A multi-physics

model was built using to model temperature profile, bead geometry and elemental

evaporation in powder bed process using a non-gaussian interaction between laser heat

source and metallic powder. Owing to the scarcity of thermo-physical properties of

metallic powders in literature, thermal conductivity, diffusivity, and heat capacity was

experimentally tested up to a temperature of 1400 degrees C. The values were used in the

computational model, which improved the results significantly. The computational work

was also used to assess the impact of fluid flow around melt pool. Dimensional analysis

was conducted to determine heat transport mode at various laser power/scan speed

combinations. Convective heat flow proved to be the dominant form of heat transfer at

higher energy input due to violent flow of the fluid around the molten region, which can

also create keyhole effect. The last part of the thesis focused on gaining useful

information about several features of the bead area such as contact angle, porosity, voids

and melt pool that were obtained using several combinations of laser power and scan

speed. These features were quantified using process learning, which was then used to

conduct a full factorial design that allows to estimate the effect of the process parameters on the output features. Both single and multi-response analysis are applied to analyze the output response. It was observed that laser power has more influential effect on all the features. Multi response analysis showed 150 W laser power and 200 mm/s produced bead with best possible features.

DEDICATION

To my lovely parents and adorable wife.

ACKNOWLEDGMENTS

I would like to thank my supervisor, Dr. Ladani. Without her constant support and guidance, it would have been difficult to produce this thesis.

I am thankful to Dr. Razmi, who has provided valuable advice time and again.

Thanks to My dissertation committee members: Dr. Kwon, Dr. Nian, and Dr. Zhuang, who have provided assistance to improve my work.

I appreciate the assistance of my fellow lab mates, specially Koushik and Jamal, who have helped me without any hesitation whenever I needed a hand.

My Mother, who has dedicated her life towards the wellbeing of her children.

My Father, who has always taken care of us from the core of his heart.

I would like to thank my brother, family, and friends, who have been there for me throughout this journey.

Last but not least, my wife, Farnaz, who also happens to be my best friend. We have shared our laughter's and struggles together.

TABLE OF CONTENTS

LIST OF TABLES

LIST OF FIGURES

CHAPTER 1

INTRODUCTION

Additive manufacturing (AM) has become a state-of-the-art process that builds three dimensional metallic parts by fusing metallic powders in a layer-by-layer approach. This process is getting widespread acceptance as it can create intricate parts that are either difficult or impossible to build using conventional techniques [1]. Powders, sheets, and wires are commonly used as feedstock materials which are consolidated to build the final part. Previously, AM was not considered for large scale production of parts. But as the process is improving over time owing to extensive research efforts, days are not far ahead when AM will be used for high volume production. Although AM is the focus of multiple manufacturing industries, this technique is of best use for medical, aerospace, automotive and defense industry as they need to manufacture parts with higher intricacies.

Two different approaches are adopted when it comes to metal AM; direct energy deposition (DED), where the feedstock material passes through a set of nozzles and is heated by a laser or electron beam heat source and powder bed fusion (PBF), where the powders are spread over a build platform. Present work is mainly focused on Powder bed fusion (PBF) process. PBF is getting increasingly widespread recognition for its ability to produce components with complex geometry. Three dimensional Parts are produced through this process in a layer after layer manner which experiences rapid heating, melting, fluid flow, re-melting of the previous layer and cooling during the process. Metallic powders are spread over a substrate and laser or electron beams are used to selectively melt the powders in this process. The flexibility of the process allows to build part ranging from mm^3 to m^3.

Many researchers have concentrated on the powder bed process motivated by its potential to produce high quality parts [1]–[10].

This process is conducted using either laser or electron beam power source. Laser and Electron beam have different working principles. Laser works optically (thus mainly following the physics of optics where reflection, absorption and transmission are dictated by these coefficients), while high speed electrons interact with the powder in Electron beam. This study dealt with selective laser melting process (SLM). In this process, the powder particles get fully melted when they interact with laser beam as opposed to selective laser sintering (SLS) where powders are partially melted. Temperature during this process can get really high due to the use of concentrated energy source. Melt pool created during the laser-powder interaction can also take different shape and size depending on various parameters such as laser power, scan speed and layer thickness etc.

1.1. Background and literature review

1.1.1. Additive Manufacturing Processes

AM process is a general term that engage in producing parts by fusing layers of materials together. In conventional machining techniques, the part is built by cutting a block of material as per the design requirements. Additive technology is completely opposite in nature as it adds layers to produce the final build. Initially, it was referred as 'Rapid Prototyping' as it was mainly used to make prototypes of the models. Now a days, this technology is rapidly moving towards full scale production due to the advancement in research and technology, and as such is termed as 'Additive Manufacturing', or '3-D printing'. AM holds a number of advantages over the subtractive techniques. As this

process does not require any special molds or tools, the build time is faster compared to other techniques. The time and cost required to production changeover is thus avoided as well [11]. Moreover, AM enables flexibility in design, which is often not possible through traditional manufacturing. For example, lattice structures are efficient as they have supreme strength accompanied by lower mass. Injection molding is effective in building solid pieces, but it becomes fragile when lattice structures are incorporated. On the other hand, AM has higher capability to accompany these structures efficiently. Innovative designs are also convenient due to the flexible design of freedom, which opens the path towards customized production. It is also easier to consolidate an assembly into a single part, thus saving inventory cost. Because of its ability to produce low density parts, AM is used in the aerospace and automotive industries extensively. Due to the additive nature, it also produces less waste, which contributes significantly to environmental sustainability during production. However, a comprehensive analysis from raw material production to the use of the final products is still needed before we can call it a 'green technology'. Some of the additive processes are described below. Only powder bed fusion process is described in detail which is relevant to this thesis.
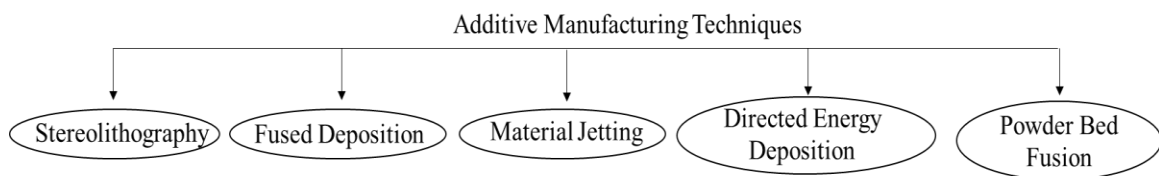
Figure 1: Additive Manufacturing Processes [12]

1.1.1.1. Powder Bed Fusion

Powder Bed Fusion (PBF) is one of the most popular forms of metal AM processes. Direct metal laser sintering, Selective laser sintering, Multi Jet Fusion, Electron beam melting,

Selective laser melting, and Selective heat sintering are the main types of powder bed fusion. Metal powders such as Inconel, Ti6Al4V, Stainless Steel etc. are spread over the building platform though a powder hopper. A laser or electron beam heat source then melts the specific portion of powder dictated by a CAD design. The power particles melt and subsequently solidify to form one layer of the build. The building platform then moves one direction along depth, and a fresh layer of powder is spread to be melted by the heat source. This process repeats until the final material is built. This process is popular in aerospace, automotive industries due to its ability to produce complicated shapes with low amount of surface roughness. Metallic powder-bed based processes can be divided into two categories: material binder and melting/sintering. In material binder methods the powder bed consists of two materials, a binding material, and a structural material. The source beam acts to melt the binder material and capillary forces draw the molten binder between the structural powder particles. As the binder solidifies it holds the structural particles together to create a cohesive layer. At this point the part may be in its final form, or a variety of post-processing procedures may be required. If the bound part is held at elevated temperature for sufficiently long time, the structural particles will sinter together through a mass diffusive process and the binder material may be removed without losing part structure [13]. Issues with the binder processes include increased porosity and decreased strength in the final part [14]. In melting/sintering methods only one material is present in the powder bed. The material is either sintered or fully melted to form a continuous layer. Sintering processes lead to parts that are high in porosities and exhibit low mechanical strength. In melting process, the powder is fully melted, and manufactured parts have no or few porosities. Optimization parameters are crucial in full melting processes as the

higher temperatures lead to shrinkage and thermal distortion [15]. This research focuses on full melting processes as they allow production of fully dense parts with satisfactory mechanical strength.
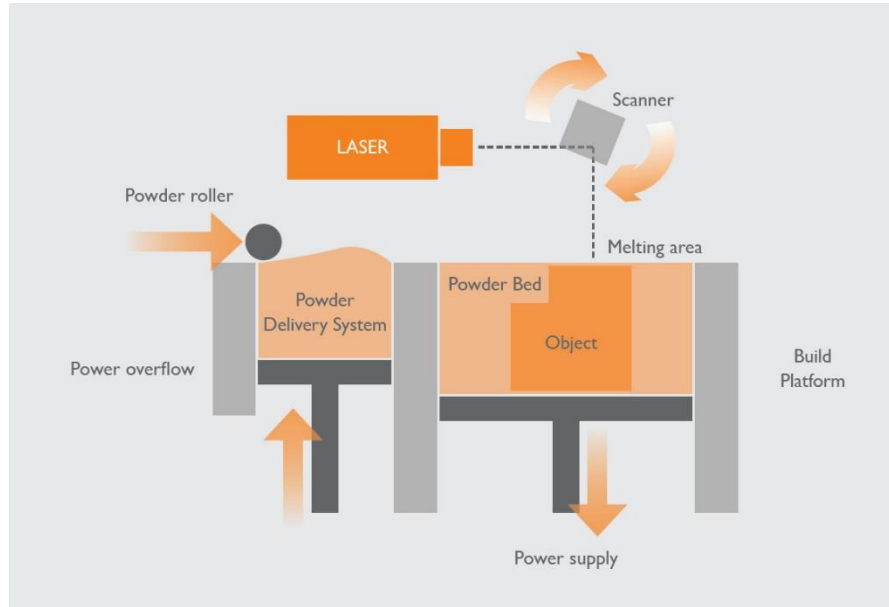
Figure 2: Powder Bed Fusion Process [16]

1.1.2. Process Parameters

Process parameters are key aspects of an AM process. Process parameters predominantly dictate how the metal powders will melt and solidify to make the final part with desirable material properties. A fully melt powder bed provides less porosity inside the build, which ensures parts with higher strength, improved ductility, and superior fatigue properties with low surface roughness.

Laser power and scan speed are two of the most important process that work simultaneously to produce parts with good quality. Laser power is the energy input per unit time from the laser source [17]. If the power is low, it will melt and solidify the powder bed quickly, creating a small melt pool. There will be less turbulence, possibly entrapping

5

low amount of vapor plumes. On the negative side, low power will likely fail to fully melt the powder bed and the layer beneath it and will leave some powder partially or fully unmelt. These powders can create excessive porosity, resulting in delamination. On the other hand, high laser power at a certain can speed will ensure fully melt powders. But excessive power can create too much penetration, which can lead to keyhole formation. Inert gases present in the processing chamber can get trapped in the keyhole region and create void. Repeated melting of the same layer can also change the microstructure of the part [18].

While fast scanning of the powder bed will ensure quicker creation of the parts, which will certainly benefit the clients in commercial scale production, this can pose certain threats to the part quality. High scan speed can create high surface tension gradient, which can lead to formation of separate balls, crating voids between them. So, an optimum combination of laser power and scan speed need to be chosen to create the best energy density that ensure proper melting and solidification.

Layer thickness is another parameter that calls for attention. Thicker layer accompanies faster production of material. But high laser power is required to ensure that the layer is fused properly. A practical range of value for layer thickness is 30-90 microns for laser power up to 500 W [17].

Hatch space is the distance between two consecutive scans of laser in parallel direction. A certain degree of spacing is maintained to remelt some part of the previous scan to ensure proper adhesion between the two scans. To have a larger hatch distance, a large spot size is required to avoid porosity between two consecutive scans.

Spot size of the laser needs to be adjusted before starting the process as most of the equipment's don't have the capability to change the beam diameter in the middle of process. Melt pool tracks are usually wider than the spot size.

Electron beam melting is usually accompanied by preheat temperature to reduce the high thermal gradient.

Powder particles size is another parameter to consider. Smaller particle and denser distribution ensure proper sintering and shallow melt pool. Larger particles need high laser energy to melt the powders completely.

1.1.2. Thermal modeling

Due to the complications associated with the powder bed fusion process, researchers have followed different modeling approaches to understand the underlying physics of the process. I. A. Roberts et al. [19] presented a simulation technique called "element birth and death" to model multiple layers during the process, where all the elements are present from the beginning, but do not contribute to the overall matrix. Each layer is activated after the previous layer is built. Dong et al. [20] used variable material properties such as thermal conductivity, density etc. during different steps of the simulation. However, heat transfer through the bottom of the powder bed was not considered, which is not representative as heat needs to be transferred to the build plate to precisely model the process. Michaleris [21] provided "Quiet" and "Inactive" method of simulation. "Quiet" method takes into account of all the elements but allocates properties to the quiet elements such that their presence is ignored until they are activated. In "Inactive" method, elements are not taken into account until the associated material is included. He also proposed a "Hybrid Quiet Inactive" method where elements are inactive initially and then assigned to quiet mode for

each layer when they are activated. Lee et al. [22] made a computational model of single layer and two overlapping tracks assuming a pre-heating temperature of 573K. Kovaleva et al. [23] used discreet grid model to model the heat transfer through the porous layers of powder considering porosity among randomly distributed powder over the build platform. Foteinous et al [24] developed an algorithm using finite difference model to build a two dimensional model to predict the temperature history while minimizing computational cost. Yavari et al [25] used graph theory instead of meshed model to save computational time to simulate the entire process. In most of the literatures, the laser-powder interaction is modeled as a Gaussian beam where the intensity of laser decreases as it moves outward from the center of the beam. However, Horak et al. [26] conducted an experiment to observe the interaction of laser-material with the help of a high quality camera and witnessed that the profile of the beam was actually different from the Gaussian beam, with intensity lower than the Gaussian beam. So, it is important to model the laser in such a way that it represents the actual laser. The modeling applied for AM is similar to welding [27]. The main boundary conditions that need to be considered as heat source, convection, and radiation heat transfer. Heat source is typically modeled using Goldak's double ellipsoid model or gaussian beam [28]. Convection is generally assumed as free convection from the top surface [29], or by using a heightened convection intended to account for both free and forced convection [30]. Radiation is also modelled from the top surface to the outside inert environment [31]. Radiation boundary condition becomes increasingly important during laser material interaction as the heat transfer through radiation is dominant at elevated temperature.

1.1.3. Fluid flow

Accurately modeling the flow of fluid in the melt pool due to Marangoni and buoyancy effects is of great importance which affects the heat distribution, melt pool shape. There are several boundary forces that need to be considered to construct an accurate multi-physics thermo-fluid model. Surface tension driven Marangoni flow and recoil pressure are two of the most important forces to consider. Surface tension plays a significant role in melt pool where temperature gradient is prominent. For most of the materials, surface tension is low where temperature is high, and the value is high in lower temperature region. This variation in surface tension pulls the fluid from the center of the melt pool to the outer radius, termed as Marangoni flow, which is the tangential stress that acts on the melt pool due to the temperature gradient. This force can induce both conductive and convective heat flux, but convection is the dominant form of mass transfer [32]. Velocity around the molten zone can vary from high to low temperature point depending on the intensity of the Marangoni flow. Surface tension also has the tendency to shrink the surface area, which can create balling effect that is detrimental to the quality of the final part. Recoil pressure is another aspect of the process that plays a crucial role at a high energy input when the temperature exceeds the evaporation point of the material. At this point, vaporization takes place, and a large amount of heat is taken away, minimizing the temperature, and depressing the melt pool [33]. The high pressure combined with Marangoni force can create instability in the melt pool, which can form keyhole sized bead containing defects such as porosities [34]. Buoyancy can have a significant impact as well in the melt pool. As the density of a material inversely varies with temperature, it pulls liquid back from the bottom of the melt pool to the top at the center owing to the temperature gradient. Although

surface tension forces are predominant in the melt pool, the role of density gradient should not be ignored.

Marangoni flow, which takes place at the surface of the molten metal due to variation of surface tension caused by a gradient in temperature, is one of the major forces for flow of fluid within the melt pool [35]. Many researchers [36], [37] have completely ignored Marangoni flow in their model. Romano et al. [1] came up with an effective conduction coefficient approach that accounted for the thermal convection due to fluid flow inside the melt pool. However, flow of fluid around the melt pool was not modeled. Andreotta et al. [4] included mass and moment equations to take into account of the Marangoni flow.

Geometry of melt pool is an important parameter for AM processes. Melt pool geometry impacts the dimensional accuracy of the build as well as the surface roughness. Melt pool geometry impacts the residual stress in several different ways. Depth of the melt pool determines how many previous layers are melted in each cycle. This re-melting and solidification not only impact the microstructure and grain size and orientation, it also impacts the residual stress as the solidification causes shrinkage in each pass. The melt pool dimensions also impact the temperature gradient and the rate at which the material is heated and cooled which results in variation of thermal strain within the material consequently resulting in mechanical deformation and strains. If the melt pool is too deep due to high energy input, then the previously solidified layers undergo repeated melting and solidification. This can create high thermal gradient multiple times in the same layer that induces residual stress causing part distortion. On the other hand, if the melt pool is too shallow, the adhesion between consecutive layers can be poor, which can create delamination. So, it is of utmost importance to analyze the physics of melt pool

comprehensively. Fluid flow around the melt pool has a large impact on temperature profile during solidification. This in turn affects the residual stress, which causes distortion in the built part [38]. Fu et al. [39] generated a three dimensional model during SLM process and concluded that depth and volume of melt pool increases for higher laser power and lower scan speed. It was observed that for a specified combination of laser power and scan speed, melt pool dimension increases towards the upper layers of a built [40]. Considering the effect of melt pool geometry on the properties of final build, it is of utter importance to develop a well-tested model that can predict the melt pool geometry for various laser power/scan speed combinations.

1.1.4. Evaporation

Because SLM and E-beam melting use a concentrated power source on a very small region, temperatures in the process can easily exceed the melting temperature of materials significantly. It is very feasible to even exceed the vaporization temperature of some of the alloying elements during the process, locally [41]. Exceeding the vaporization temperature can cause evaporation of some of alloying elements. Evaporation of elements can change the composition of the final build. If the change in composition exceeds the permissible limit, it can adversely affect the properties (i.e. tensile strength, hardness etc.) [42]. Mukherjee et al. [42] developed an analytical model using Langmuir equation for direct energy deposition and observed that chromium experiences the higher amount of evaporation for Inconel 625. P.A.A Khan et al. [43] collected the condensate of vaporized elements through a quartz tube and examined the samples with an x-ray analyzer. They found out that manganese, iron and chromium are the most volatile alloying elements during laser welding of AISI 202 stainless steels. T. Liu [44] et al. predicted the

vaporization rate of the Knudsen layer in laser keyhole welding through an analytical model and found out that the concentration of manganese changed significantly for stainless steel. Beiranvand et al [45] studied the effect of Mg in Aluminum alloys, and found out that increase in Mg vapor plumes due to high laser input has a positive correlation with effective laser coefficient. Although the composition change in laser welding is more pronounced because of the low welding speed and high laser power involved, the importance of determining evaporation in SLM cannot be ignored as higher laser powers and lower melting material are being used in this process lately. Significant amount of work is done on evaporation in laser welding, but literature on effect of evaporation in powder bed AM is not adequate.

1.1.5. Thermo-physical properties

AM process is a complex physical phenomenon which involves interaction between powder and heat source, powder melting, flow around the molten pool and subsequent solidification. Numerical modeling helps us to understand and improve the underlying process, as well as saves experimental cost and time. A comprehensive model can provide valuable insight regarding the entire process to understand final component properties. Thermal modeling of transferring heat from powder bed to the build platform is based on the following energy balance equation [10]:

$$\rho C_p \frac{\partial T}{\partial t} + \rho C_p \boldsymbol{u}. \nabla T + \nabla. q = Q$$

Here, Q is the heat source, T is the temperature field, is the density, u is the velocity field due to fluid flow, C_p is the heat capacity and k is the thermal conductivity. So, to get a good idea of this process, it is necessary to provide accurate information about the thermal

properties of the powders. However, it is extremely difficult to measure these properties during the process itself at high temperatures. Because of the scarcity of experimental data, these computations largely depend on analytical models that tries to predict the values of conductivity and heat capacity [31], [3],[36].

1.1.5.1 Thermal conductivity

Thermal conductivity is one of the most important properties of powder as it dictates the amount of heat that is transferred during the process. When metals are heated, the closely attached atoms gain energy and start vibrating rigorously. Upon vibration, the atoms come closer to neighbor atoms and transfer some of the energy to them and thus transfer heat through conduction. Conductivity of powder is much less than that of solid as it involves porosity between adjacent particles. These gaps between the particles create a network of thermal resistance that hampers heat conduction. Several analytical models have been proposed for thermal conductivity to fill the gap due to the lack of experimental results.Schlunder et al. [46] proposed a model that only considered conductivity of the powders. They showed that considering contact between powder particles provides good agreement with experimental results. Child et al. [47] generated an equation for powder bed conductivity that depends on conductivity of the solid and density of the powder bed relative to the solid and found out that conductivity increases with increasing density. Sib and Barlow [48] considered heat transfer by free fluid, heat transfer due to partial contact between two particles and heat transfer from the powder particle to adjacent fluid in their proposed effective conductivity equation. Gusarov et al. [49] assumed that gases entrapped between the powder particles had a much less conductivity than the metals and thus considered it insignificant and concluded that contact size is the predominant force that

determines thermal conductivity. Hadley [50] proposed an effective thermal conductivity equation that could be used for un-sintered powders. Agapiou [51] introduced a correlation that was more befitting to powders that were initially sintered, typically done in electron beam melting process [EBM] where powders are preheated. Due to the sintering of the powders, adjacent particles adhere to each other more closely, increasing the contact area that leads to a higher prediction of thermal conductivity for Agapiou than the Hadley relation. Zhang et al. [52] developed a model to calculate the thermal conductivity of nanofluids considering dimensionless parameters like Brinkman number, Reynolds number and Prandtl number. Andisheh-Tadbir et al. [53] proposed a new model for microporous layers based on porosity, pore size and compression. Ling et al. [54] developed a model to predict conductivity of graphite based phase change composite based on density of the composite and fraction of mass of graphite. Other than these analytical models, several numerical approaches were also conducted by different researchers. Siu et al [55] used contact angle of neighboring powder particles with porosity ranging from 0.17 to 0.48 and relied on identification of unit cells to compute the conductivity of powder. They determined that FCC unit cells have the highest conductivity for a given contact radius. Asakuma et al. [56] used two types of unit cells (FCC and BCC) in his model and showed that effective conductivity increases non-linearly with Nusselt number. Ayatollahi et al. [57] also used unit cell approach to find the effective thermal conductivity in fractured porous media. Boomsma et al. [58] calculated the conductivity of a metallic foam using a detailed description of the three-dimensional foam geometry. Singh et al. [59] developed an computational model to predict the thermal conductivity of porous materials filled with soil, water and air between the particles and observed that conductivity varies non-linearly

14

for each of the fill. A few experimental techniques have also been introduced to calculate thermal conductivity. In laser flash technique [60] the powder surface is heated by laser beam. The temperature rise is measured by a thermocouple, which is sent to a processing software. Transient plane source (TPS) is a non-destructive technique [4] that uses a sensor element that acts both as a heat source and measures temperature rise at the same time. The hot wire (THW) [61] method is based on the measurement of increase in temperature of a hot wire immersed in the cylindrical sample which can act as an electrical heater and resistance thermometer simultaneously. Other methods have also been applied to get the thermal properties of materials [62]–[67].

1.1.5.2 Thermal diffusivity

Thermal diffusivity is another parameter which measures the diffusion of heat from hot to cold region. Bruggeman [68] developed an analytical relation to determine the effective diffusivity of packed spherical particles based on diffusivity of solid particles and porosity between the particles. Zamel et al. [69] used Bosanquet's formula that includes Knudsen and bulk diffusivity to calculate thermal diffusivity of porous layers. Andisheh-Tadbir et al. [53] developed diffusivity model for micro porous layers using unit cell approach. Abbas et al [70] investigated the effect of Ag in Cu-Al alloys, and found out that higher content of Ag increase both diffusivity and conductivity of Ag due to higher conductivity of silver.

1.1.5.3 Specific heat capacity

Specific heat capacity is another property that is essential to model the process. It is defined as the amount of heat that is needed to raise the temperature of the sample by 1 degree Celsius. There are several literatures on the heat capacity of solid metals [71], [72], but it

is limited for metallic powders. Due to the deficiency of experimental data, heat capacity values are generally assumed as same as solid metal [10], [31], [73].

1.1.6. Dimensional Analysis

The importance of fluid flow around melt pool and transport of heat due to the fluid motion can be conveniently analyzed by using dimensionless numbers like Nusselt number, Peclet number and Marangoni number [74], [75]. Nusselt number and Peclet number indicate the heat and momentum transfer respectively, while Marangoni number is defined as ratio of Marangoni flow to heat diffusion rate. The relative transport of heat through convection and conduction in the process can be assessed using these numbers. These studies can pave the path to understand the inherent physics of powder bed fusion technique in a simplistic manner as a number of variables are combined. Dimensionless numbers can reduce the complications associated with a process significantly and analyze the effect of input variables using unitless parameters [76].

1.1.7. Bead Cross-section Features

Powder bed fusion (PBF) AM process uses laser or electron beam to melt metallic powders over a building platform to print one layer of the build dictated by a CAD design. The process continues until the final product is built. Due to the variability of the process parameters like laser power, scanning speed, layer thickness etc., melt pools that generate during the process can possess distinguished features [1], [31], [77]–[79] which could be used to conduct process optimization.

Researchers have tried to analyze the characteristics of different aspects of the build to optimize the parameters that can influence the process. Geometrical feature such as contact angle between the present and the previous layers, which dictates the wetting behavior of

16

the melt pool has been studied by a number of scientists. Fateri et al [80] investigated the effect of temperature and viscosity towards the evolution of contact angle using Hot stage Microscopy. The study showed that contact angle decreases as the powders start to sinter at higher temperature points. Yuan et al. [81] discussed various techniques like drop-shape analyzer, Wilhelmy balance method etc. to measure contact angle. Haley et. al [82] used computational fluid dynamics (CFD) simulation technique to observe the influence of particle size, melt pool shape, surface tension on wetting dynamics. They found out that powder particle residence time, which is termed as the time between interaction of powder and heat source, and complete melting, is dependent on particle size and surface tension, and contact angle varies inversely with residence time. Triantafyllidis et al [83] established a relation between surface roughness and contact angle and deduced that roughness increases with reduced contact angle. Development of defects in AM has been a major concern and a hindrance towards large scale production. A lot of research has been dedicated towards the physics behind the formation of these defects. Brennan et al [84] discussed about different defects like porosity, voids, lack of fusion defects and how they can be reduced using hot isostatic process (HIP). Murakami et al. [85]studied the effect of surface roughness and defects in on fatigue properties. Sanaei et al. [86] analyzed the defects in AM part based on specific locations like neck and at the perimeter of the samples. They used K-S statistical test to show that the distribution of defects are different in the neck and perimeter region. Keyhole induced large voids inside the melt pool has also been discussed in some work [6]. Other papers [16], [17] have also tried to investigate defects from different perspective. These papers mainly focused on the formation of defects on the

17

build direction. Analysis of these defects along the bead cross section based on process parameters like laser power and scan speed is largely missing from the literature.

1.1.8. Process Parameter Optimization

Traditionally, process parameter optimizations are implemented using computational methods [31], [87]. Although computational modeling can reveal important information about melt pool, microstructure, temperature history etc. that change with the input variables, due to the complications in the process, these models possess a lot of simplified assumptions, which results in deviation from actual experimental results. To solve the issue, many researchers have recently opted to use machine learning algorithm techniques to optimize the process parameters. Kwon et al [88] used convolutional neural network (CNN) to predict laser power from melt pool images taken during the experiment, and built a model with 96% accuracy. Caiazzo et al [89] built a three layer cascade forward propagation artificial neural network (ANN) to predict the process parameters to obtain specified built geometry. They produced result with 2% error for laser power, 5.8% for scanning speed, and 5.5% for powder feeding rate. Although machine learning models have become increasingly popular as they can predict data with high accuracy, these techniques are still not good enough to predict process parameters with smaller datasets. These techniques require a large number of experimental data set to train the models, which is both time consuming and expensive. Statistical analysis techniques have also been employed to identify patterns in engineering [90]. Sanaei et al. [16] analyzed the defects in AM part based on specific locations like neck and at the perimeter of the samples. They used K-S statistical test to show that the distribution of defects are different in the neck and perimeter region. Keyhole induced large voids inside the melt pool has also been discussed

in some work [17]. Baturynska1[18] tried to optimize the dimensional accuracy of additively manufactured parts using statistical analysis. They found out that STL model properties (number of mesh triangles, surface, and volume of CAD model) have significant effect on length, width and thickness of the build. Casalino et al. [19] investigated the impact of laser power and scan speed on mechanical properties such as hardness, tensile strength of the final build. They found out that increasing energy density decreases surface roughness and increases hardness. Whip et al [20] used analysis of variance method to observe the effect of process parameters in melt pool and surface roughness. They found out that increasing laser power increases the melt pool size, which facilitates in smoother surface due to proper wettability.

1.2. Gap in literature

Temperature profile created during the interaction of laser and powder bed is of great significance as it impacts the melt pool geometry, which dictates the microstructure of the build. Majority of the literature characterizes the laser following a Gaussian beam, where the intensity of the laser is maximum at the center and decays exponentially as it goes radially outward. To model the process appropriately, laser behavior needs to be implemented in a way that the properties of laser such as beam quality factor, wavelength, and waist radius can be taken under consideration. A realistic laser-powder interaction with appropriate fluid flow behavior around the melt pool is missing from the literature.

As temperature during the process can reach the evaporation temperature of some of the alloying elements, which can change the final composition of the build, affecting the

material properties adversely. Significant amount of work is done on evaporation in laser welding, but literature on effect of evaporation in powder bed AM is not adequate.

As the thermo-physical properties are sensitive to temperature, it is of paramount importance to accurately input these values in the modeling efforts. Experimentally obtained values for heat diffusivity, thermal conductivity and heat capacity for metal powders are very limited in the literature. Again, although conduction heat transferred was considered to be the main transport of heat [36] recent modeling efforts have showcased the fact that convection also plays a vital role in the melt pool [91]. Despite the development of a lot of modeling & simulation in recent times, a comprehensive thermo-fluid modeling including experimentally obtained thermophysical properties of powders is needed in literature.

Although there are several works done on the defects found in additively manufactured parts in the scanning plane, they are not well recognized in the melt pool cross section. Quantification of these defects/ features for different combinations of process parameters like laser power and scan speed and a thorough statistical analysis to optimize the process parameters are also rare in the literature.

1.3. Problem Statement

Although many research work have focused on modeling the powder bed fusion process, there is still a need of a comprehensive multi-physics approach that includes a realistic interaction between the laser heat source and powder material. Moreover, current literature also lacks experimental data for thermo-physical properties at elevated temperature that is crucial to accurately model the process. Process parameter optimization has been another

key factor in the powder bed process. Although computational modeling and machine learning approaches have been conducted, there is still a lack of parameter optimization in terms of all the features like contact angle, porosity, melt pool size etc. of the bead at the same time. So, a multi response analysis is needed to optimize the key parameters like laser power and scan speed.

1.4. Research objective and Approach

The primary objective of this research is to build a robust multi-physics computational model with a realistic laser-powder interaction process along with experimentally obtained thermo-physical properties and proper boundary conditions that enables a better understanding of powder bed fusion AM process. A comprehensive single and multi-response statistical analysis is also conducted of different features such as contact angle, porosity, melt pool area, void etc. along the bead cross section optimize main process parameters; laser power and scan speed. The research approach followed to achieve the objectives are shown in **Figure *3***
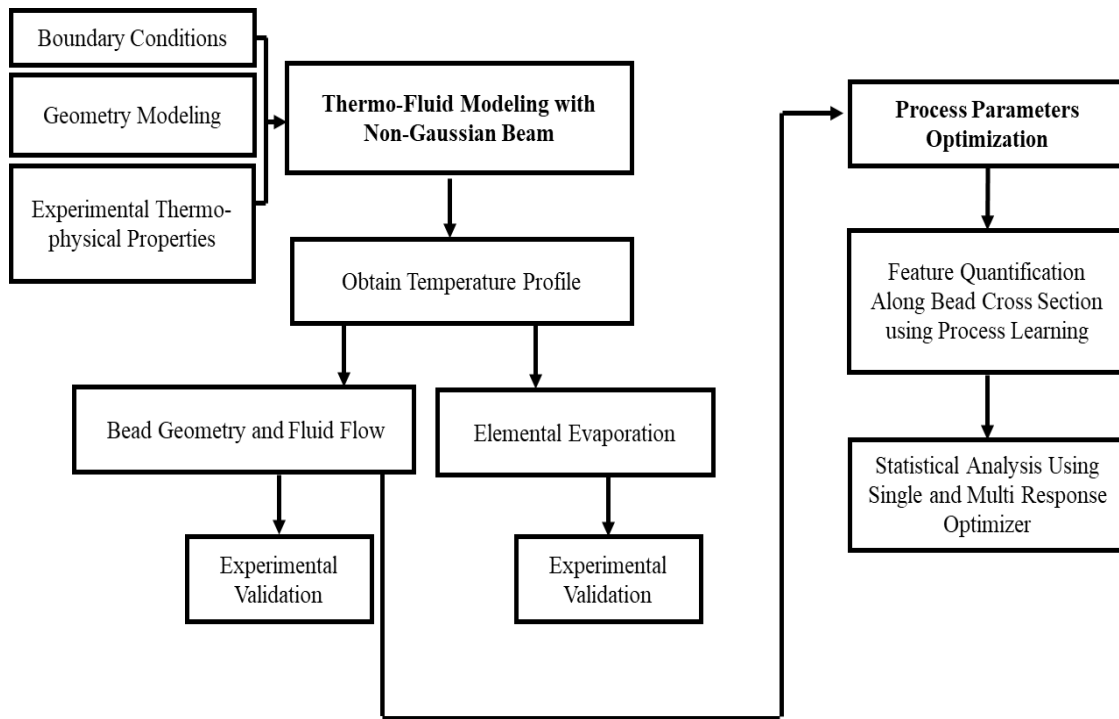
Figure 3: Research Approach

CHAPTER 2

MULTI-PHYSICS MODELING

This chapter provides a detailed description of the computational modeling that lays the foundation of this thesis. A comprehensive thermo-fluid analysis is conducted using heat transfer and CFM modules to understand the underlying mechanism of the powder bed process, as well as to validate the model against experimental results. Temperature profile is obtained using non-gaussian interaction between laser and powder. The temperature history is utilized to get the bead geometry using a process called level set method. Elemental evaporation of the metal powders are also analytically calculated.

2.1. Laser Heat Source

Most of the literature on modeling laser beam melting process deals with modeling laser as a heat source on the surface of the material. The intensity of the heat source is typically considered to follow a Gaussian distribution, in which the heat intensity is maximum at the middle of the beam and decreases exponentially as it goes radially outward. This work aimed to approach the laser-powder interaction equation in a way that represents the actual laser profile in a more comprehensible way. A Gaussian distributed laser beam is defined as [92]:

$$I(x, y, z) = \frac{2P}{\pi * w(z)^2} * \exp\left[-\frac{2 * (x - vt)^2 + y^2)}{w(z)^2}\right] \tag{1}$$

$$w(z) = w_0 * sqrt\left[1 + \left(\frac{\lambda * z}{\pi * (w_0)^2}\right)^2\right] \tag{2}$$

Here, w (z) is the beam radius at a depth z, w_0 is the beam waist radius, t is the laser scan time, and λ is the laser wavelength. Beam waist is the location at which the radius of the beam is minimum. In most of the literature, beam radius is assumed to be equal to w_0. The

beam that follows a Gaussian profile is highly concentrated towards the focus of the beam, thus creating a very high temperature at that point. But, it was observed that the actual beam is not as highly focused as a Gaussian beam [93], making the temperature profile lower than the Gaussian one. For lasers with low power, the beam profile can be similar to Gaussian beam, but the eccentricity of the beam profile increases with increasing laser power. To differentiate between a Gaussian or ideal beam with a non-Gaussian beam, a new parameter called beam quality factor is used, which is denoted by M^2. The value of M^2 for ideal or Gaussian beam is equal to 1. It is more than 1 for a non-Gaussian beam. For high laser power, this value can reach up to 10 or more [94]. With the introduction of this quality factor, the laser can be modeled in a more appropriate manner. The beam quality factor is defined as [95]:

$$M^2 = \text{BPP} * \frac{\pi}{\lambda} \tag{3}$$

Where BPP is "beam parameter product" and is the product of beam radius (w_0) and the beam divergence (Θ). Yb-fiber laser was used which had a wavelength of 1064 nm. Including the M^2 factor, equation (2) is rearranged as [94]:

$$w(z) = w_0 * sqrt[1 + \left(\frac{\lambda*z*M\^2}{\pi*(w_0)^2}\right)^2] \tag{4}$$

This equation was used in this work to model the laser-powder interaction.

2.2. Modeling Technique

The modeling strategy consists of two sets of models. A 3-dimensional finite element model utilized to determine the temperature history through thermal modeling combined with fluid dynamic modeling inside the melt pool region. The second model is two dimensional having a cross section of the material as the laser crosses a region. This 2D

24

model is used to obtain the geometry and shape of the bead. The temperature history is extracted from the 3D model is applied to the 2D model as thermal load. The 2D model utilizes the level set method to obtain the bead geometry of the solidified part.

The 3D model and meshing are presented in. As it can be seen from the figure, there are three distinct regions in the model: substrate made of stainless steel with a thickness of 1 mm upon which the process was completed, 0.9 mm of solid portion in the middle which was melted and subsequently solidified and 0.04 mm of freshly spread powder on the top that is to be melted by the laser. The domains had a length of 9 mm and width of 3 mm each. Symmetry in the Y direction was used to save computational time. So, half of the model was built along that direction. Radiation boundary condition was applied to the powder surface.

$$q = \varepsilon * \sigma * (T^{amb} - T^4) \tag{5}$$

Here $\varepsilon = 0.87$ is the surface emissivity [48]. $\sigma = 5.67 \times 10^{-8}$ W/m^2.K^4 is called the Stefan-Boltzman constant, q is the heat flux and T^{amb} is the temperature of the surrounding atmosphere. Adiabatic boundary condition was applied to the bottom of the build plate and side domains.
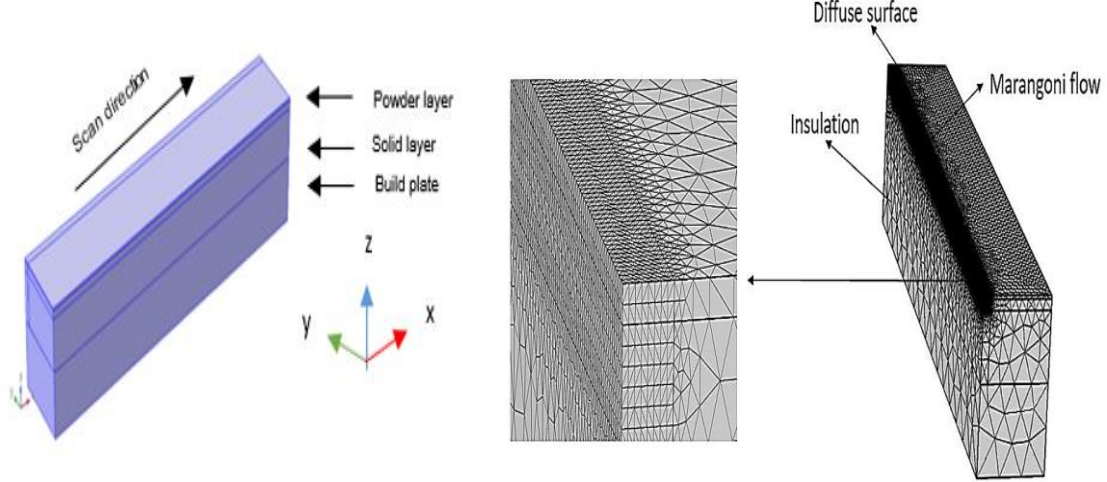
Figure 4: 3D Model Set Up, Boundary Condition, Dimensions, and Mesh to Model Temperature Profile

The governing energy, mass and moment balance equations are:

$$\rho C_p \frac{\partial T}{\partial t} + \rho C_p \boldsymbol{u}.\nabla T + \nabla.q = Q \tag{6}$$

$$\rho \frac{\partial u}{\partial t} + \rho(u.\nabla)u = \nabla.[-pI + \mu(\nabla u + (\nabla u)^T)] + F \tag{7}$$

$$p\nabla(u) = 0 \tag{8}$$

Equation (6), (7) and (8) denote energy, moment and mass balance respectively. Here, u is the velocity field, Q is the heat source, T is the temperature field, ρ is the density, Cp is the heat capacity, q is the heat flux, μ is the dynamic viscosity, p is the pressure, F is the force due to fluid flow. Heat transport was associated with the energy equation and mass and moment accounted for the fluid flow in the molten region. In this work, the calculated Reynolds number around the melt pool varied from 0.00054 (Lowest, 150W/1200mms) to 52.6 (Highest, 300W/200 mms) for different laser power/ scan speed combinations. As the Transition Reynolds number from laminar to turbulent region is Re=600 [37], laminar model was used in the simulation. Marangoni flow, which is caused by surface tension

26

variation within the melt pool contributes to the melt pool dynamic significantly. The surface tension variation is caused by the temperature gradient within the melt pool. Marangoni number is given by [96]

$$Ma = \left(\frac{\partial \gamma}{\partial T}\right) . \frac{L.\Delta T}{\mu.\alpha} \tag{9}$$

Here, γ is the surface tension, α is the thermal diffusivity, L is the length scale of the melt pool, μ is the dynamic viscosity.

Table i: Process Parameters

Process parameter	Value
Laser power (W)	100, 150, 200
Scan speed (mm/s)	200, 700, 1200
Layer thickness (µm)	40
Beam waist radius (µm)	100
Penetration depth (µm)	140

2.3. Bead Geometry

A second model (*Figure 5)* was built to get the bead geometry of the build. The model was two dimensional that consisted of the melt pool, the location of which was extracted from the 1st model, where the temperature was maximum and the outside nitrogen atmosphere. The interface of the melt pool and atmosphere was traced by a process called level set method. The process started as soon melting started and finished when the melt pool solidified under the effect of surface tension and gravity.

27
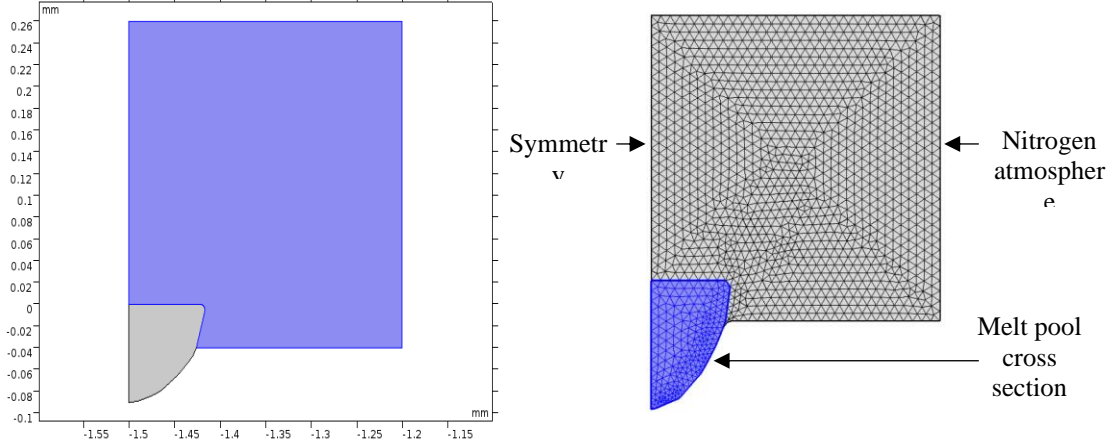
Figure 5: 2D Model Geometry and Mesh

Level set method uses the following equations:

$$\nabla GI.\nabla GI + \gamma. GI(\nabla.\nabla GI) = (1 + 2\sigma_w)GI^4 \tag{10}$$

$$\frac{\partial \emptyset}{\partial t} + \nabla.(u\emptyset) = \lambda\nabla.\left(\in_{ls}\nabla\emptyset - \emptyset(1-\emptyset)\frac{\nabla\emptyset}{|\nabla\emptyset|}\right) \tag{11}$$

Here, GI is the reciprocal interface distance, γ is the surface tension, u is the velocity field, λ is the reinitialization parameter, $\in_{ls}$ is the parameter controlling interface thickness, $\emptyset$ is The level set variable. At the beginning of the level set method, $\emptyset$ is 0 for the molten region and 1 in the atmosphere, which gradually changes. The properties i.e. viscosity and density are different on molten pool area and atmosphere. So, when the interface is crossed, there is abrupt change in these properties, which means there is a sudden change in $\emptyset$. This sudden change causes numerical instability in the simulation. To avoid that, the coding is so done that this property change takes place smoothly across a finite width in the interface region. This width is denoted by $\in_{ls}$. Reinitialization is used in level set method to avoid numerical deterioration of the interface. As time progresses, there might be some discontinuity in the zero-level set function $\emptyset$. To get rid of that, $\emptyset$ is updated (reinitialized) after certain number of iterations. λ determines the required amount of reinitialization or

28

stabilization. If λ is too small, there might be oscillation in $\emptyset$, while a too large value of $\emptyset$ makes the interface move incorrectly with time. Hence, an optimized value of λ has to be used. The parameters used in this work are: γ_m= 0.018 N/m at melting temperature, λ=.4 m/s, ϵ_{ls}=0.005 mm [97].

2.4. Material Properties

Powder, molten metal and solid metal of Inconel 718 was used for this simulation. As the temperature changes, the properties are updated and changed as the phases of material change. Powder is one of the most difficult materials to be modeled. Properties of metallic powder is not readily available in literature. For example, thermal conductivity of metallic powders, are typically modeled using analytical or numerical models. However, most of these theoretical models are function of many parameters. To avoid the variability of these models and to realistically model the powder materials, actual thermal conductivity properties are obtained experimentally for this study. The experiments are conducted using an instrument called transient plane source (TPS-2200). TPS-2200 can quickly and accurately measure the thermal conductivity of metallic powder through a non-destructive process. The thermal conductivity values attained with a packing density of 5.46 g/cm^3 were chosen for the present study. Temperature dependent thermal conductivity of solid Inconel 718 and steel was taken from mills [98] .

The equation used for calculating the dynamic viscosity was taken from literature [99]

$$\mu(mPa * s) = .196e^{\frac{5848}{T}} \tag{12}$$

Temperature dependent specific heat and density values were imported from mills [98].

The values of density of powder were chosen to be 5.46 g/cm3 with a porosity of 0.3.

Surface tension was obtained from Lee et al. [100]

$$\gamma(T) = \gamma_m + d\gamma/dT * (T - T_m) \tag{13}$$

Temperature dependent absorptivity of Inconel 718 alloy was taken from literature, which

varies from 0.3 to 0.55 [99].

2.5. Modeling Elemental Evaporation

Vaporization flux of elements of an alloy is determined by the Langmuir equation [101]:

$$J_i = \frac{P_i}{(2*\Pi*R*M_i*T)^{\frac{1}{2}}} \tag{14}$$

Here, P_i is vapor pressure of each element in the alloy, R=8.314 J/mol.K is the universal

gas constant, M_i is the molecular weight of element i, T is the maximum temperature

generated during the laser-material interaction. It was observed experimentally that the

Langmuir equation over predicts the vapor flux by 5 to 20 percent [101], as it does not take

into account of the mass that condensates back to the surface. To get rid of the error, J_i is

multiplied by β =0.05 [42], a fractional value considering the condensation:

$$J_i = \frac{\beta*P_i}{(2*\Pi*R*M_i*T)^{\frac{1}{2}}} \tag{15}$$

The vapor pressure P_i is obtained from the following equation [102]:

$$\log(P) = A + \frac{B}{T} + C\log T + \frac{D}{T^3} \tag{16}$$

Here, the constants A, B, C and D are different from each element. It can be seen that, vapor pressure is heavily influenced by the melt pool temperature. The mass of the vaporized elements is:

$$\Delta m_i = J_i * A_s * t \tag{17}$$

Here A_s is the area of the melt pool, which was determined with COMSOL, t is the laser scanning time.

Final concentrations of the elements is [42]:

$$W_f = \frac{V*\rho*W_i - \Delta m_i}{V*\rho - \sum \Delta m_i} \tag{18}$$

Here, V is the volume of the deposited material, ρ is the density and W_i is the initial concentration of the element. Volume was determined by multiplying the cross-sectional area of the melt pool by the length of the track.

2.6. Results and Discussion

2.6.1. Temperature Profile:

Figure 6 shows the temperature profile of non-Gaussian and Gaussian beams. Gaussian beam generates a more localized profile of temperature which causes a higher temperature build-up at the center of the melt pool, as is evident from the figure. Comparatively more uniform distribution of heat, away from the center of the beam is observed with the introduction of beam quality factor since the quality factor reduces the beam focus. As the quality factor distorts the behavior of an ideal Gaussian beam, the heat is no more highly concentrated at the focus of the beam. With further increase of the quality factor (M^2), deterioration of beam quality is observed which represents a more realistic beam nature.

31

This emphasizes the fact that incorporating the M^2 factor is important to model the true interactive behavior of material and laser.
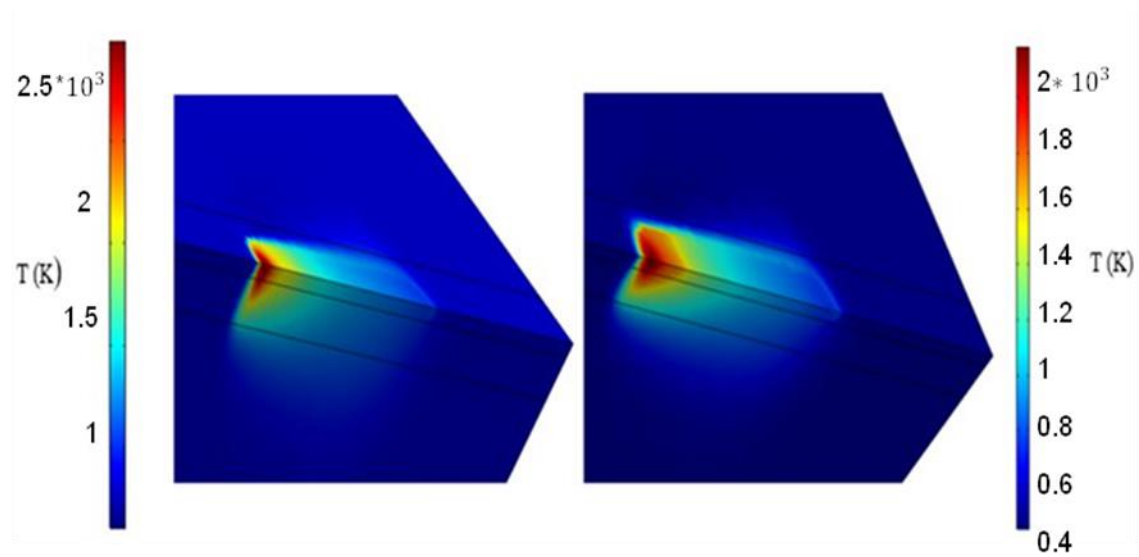
Figure 6: Melt pool and temperature distribution for (i) Gaussian and (ii) non-Gaussian beam

To validate the temperature profile, an alternate geometry was modeled with a length of 60 mm, width of 5 mm and height of 25 mm. The experiment was conducted with 180 W laser power and 600 mm/s scan speed [103]. An MCS 640 thermal imager was used to measure the temperature at the laser-powder interaction zone. *Figure 7a* shows a comparison between the non-Gaussian and Gaussian beam model when they were compared against experimental result. The profile obtained with non- Gaussian beam was more similar to the experimental temperature profile with a lower maximum temperature than Gaussian beam. The spikes in the experimental data in the lower temperature range is due to the inability of the camera to measure temperature in the lower range. The laser profile could not be obtained from this specific literature. However, as the temperature profile of the non-

Gaussian beam was similar to the experimental result, it can be expected that the laser profiles would agree as well.
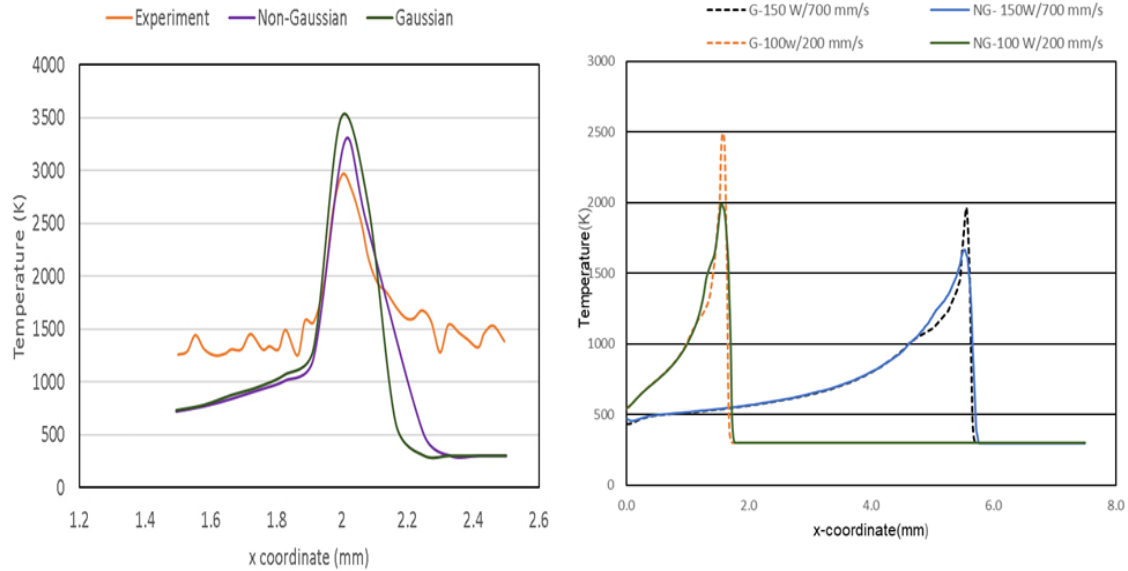
Figure 7: (a) Comparison of temperature profile for Gaussian and non-Gaussian beam versus experiment, (b) Variation of temperature profile for various speeds and powers compared in Gaussian and non-Gaussian beam profiles.

Figure 7b presents temperature profile of both non- Gaussian and Gaussian beam for different laser power/ scan speed combinations and all of them shows a lower temperature profile for the non-Gaussian beam. Due to the high concentration, both temperature and intensity are higher at the focus for the Gaussian model for all three combinations. For 150W/700 mm/s combination, the high speed allows shorter time span of interaction between laser and powder which results in lower intensity and temperature profile. On the other hand, the maximum temperature is higher in 300W/700 mm/s combination than in 100W/200 mm/s due to considerably higher power in the former combination despite the

later having a lower scan speed; this indicates that power plays the dominant role over scan speed for all combinations. Temperature goes above 1443k, the assumed melting point of Inconel 718, for all combinations of laser power and scan speed.

2.6.2 Bead Geometry

Figure 8(a) presents a graphical comparison between the bead geometry of the model and experiment. The experiment [5] was conducted using EOSINT M 280 machine. 24 square Inconel 718 specimen having block dimensions of 25.4 mm×25.4 mm ×4.0 mm was manufactured. Each of the specimen were fabricated using different sets of combinations of laser power and scan speed. The laser scanned 10 equally spaced lines to analyze the variations of process parameters. Images of the cross-sectional area were taken to investigate the melt pool geometries.
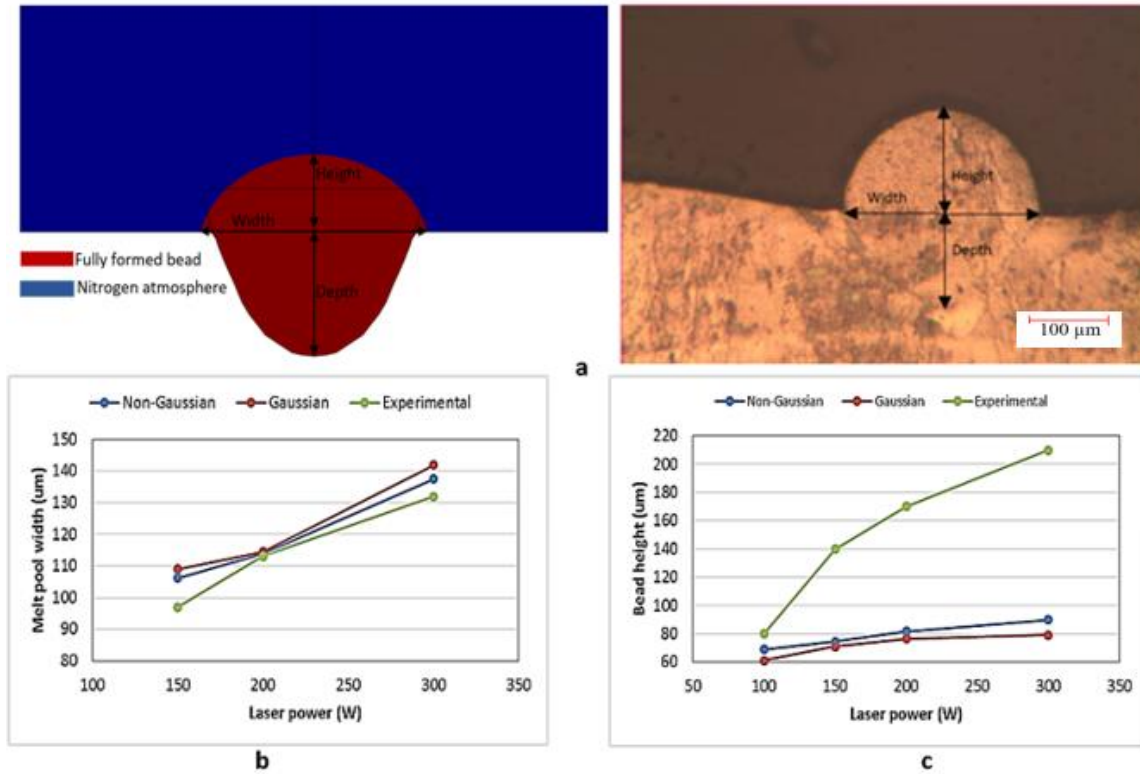
Figure 8: (a)Simulated and experimentally obtained bead cross sections for laser power = 100W and scan speed = 200 mm/s, (b) Melt pool width comparison at a scan speed of 1200 mm/s and (c) Bead height comparison at a scan speed of 200 mm/s.

The following paragraphs compare the bead geometry for non-Gaussian beam with M^2 factor, Gaussian beam [4] and experimental results.

Table ii presents a comparison of width of the melt pool between non- Gaussian and Gaussian beam models against experimentally observed data. The results show that the non-Gaussian beam results were more accurate than the Gaussian beam. The temperature was lower around the melt pool for non-Gaussian model, making the width of the melt pool smaller. Results acquired with higher scan speed provided more accurate results for both models.

Table ii: Melt pool width

Width(um)	Non-Gaussian beam				Gaussian beam				Experimental results				Difference with experiment- Non Gaussian/ Gaussian model			
	100 W	150 W	200 W	300 W	100 W	150 W	200 W	300 W	100 W	150 W	200 W	300 W	100 W	150 W	200 W	300W
200 mm /s	162.1	221.3	263	340	181	227.5	284	367	154.2±14.6	204.± 11	223 ±14.8	295 ±23.9	5.12%/ 17.3%	8.48 %/ 11.5%	17.93 %/30 %	15.47 %/24.4 %
700 mm /s		120.5	127	176.4		122	129	194		118 ±5.	144.±9.2	185 ±12.1		1.68 %/ 3.38 %	- 13%/ -10%	-4.8%/ 4.8%
1200 mm /s		106.12	113.92	137.5		109	114.5	142		97± 8.1	113.±11.9	132.2±10.6		9.4% / 12.4 %	0.8% / 1.32 %	4%/ 7.4%

Bead heights could be obtained for only those experiments which were conducted with a scanning speed of 200 mm/s. Higher scan speed shapes were partially distorted due to balling effect. Comparison against experiment showed that non-Gaussian beam model performed better than the Gaussian beam model in predicting the bead height; it is expected that the same trend will be observed in case of higher scan speed as well. It can be observed that there is a considerable difference between the experimental and simulation results for bead height for scan speeds of 200 mm/s. The experimentally measured values of bead height at this speed is significantly larger than layer thickness (40 um), which leads this researcher to believe that some errors were associated while measuring the bead height and the simulated results were reasonable.

Table iii: Bead Height

	Non-Gaussian beam				Gaussian beam				Experimental results				Difference with experiment- Non Gaussian/ Gaussian model			
Height (um)	100 W	150 W	200 W	300 W	100 W	150 W	200 W	300 W	100 W	150 W	200 W	300 W	100 W	150 W	200 W	300 W
200 mm/s	69	74.5	81.8	90	61	71	76.5	79	80	140	170	210	13.75%/23%	46.8%/49.2%	51.88%/55.%	57%/62.4%
700 mm/s		70.5	74	82.2		43.5	63.1	94.3								
1200 mm/s		63.5		66.8	59.2		66.1									

Figure 8b and *Figure 8c* shows comparison of melt pool width and bead height at 1200 mm/s and 200 mm/s scan speed respectively for Gaussian model, non-Gaussian model and experimental data. There is a large difference between the simulated models and experimental data for bead height. There could be error in the measurement of the bead height due to the formation of balling and other defects, which could be attributed to the large discrepancy between the measured and simulated data.

For melt pool depth, Gaussian beams results were slightly better than the non-Gaussian beam.

Table iv: Melt Pool Depth

	Non-Gaussian beam	Gaussian beam	Experimental results	Difference with experiment- Non Gaussian/ Gaussian model

Depth (um)	100 W	150 W	200 W	300 W	100 W	150 W	200 W	300 W	100 W	150 W	200 W	300 W	100 W	150 W	200 W	300 W
200 mm/s	73.4	106	129.2	161.3	85.6	111.3	131.2	162.8	148.1±0.3	215.7±67.5	280.5±48.6	299.1±149	50.4%/42.2	50.86%/48.4	53.9%/53.2	46.1%/45.5
700 mm/s		35.6	50.6	87.2		40.4	58	91		48.2±1.3	64.4±18.2	96.5±24.7		26.1%/16.2	21.4%/9.83	9.6%/5.7
1200 mm/s			40	60.5			40.8	64.4			41.5±9.8	101.1±37.2			3.61%/1.7%	40.2%/36.3

2.6.3. Composition Change

Figure 9a shows concentration changes for different elements for a constant power of 300 W and 3 different scan speed: 200, 700 and 1200 mm/s. It is evident that for lower scan speed the composition change is the highest as the temperature is high for those combinations of laser power and scan speed. Consequently, the vapor pressure also increases considerably, which helps to evaporate the metals. On the contrary, laser does not get much time to interact with surface in case of higher scan speed, resulting in very low concentration change. The concentration change for Chromium is highest, with a change of .2255%.

a

b
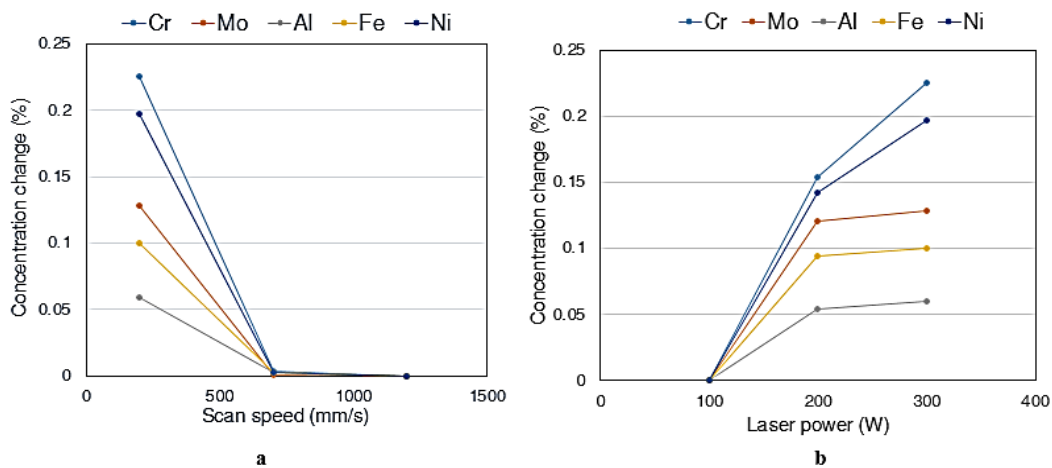
Figure 9: Change in Concentration of Elements for (a) Varying Scan Speed, (b) Varying

Power.

Figure 9b demonstrates the concentration change for different elements for different powers at 200 mm/s of laser speed. As the power increases, the concentration change is more evident. Chromium and nickel undergo maximum change in concentration. It can also be observed that, only aluminum and iron exceeds a small amount than the permissible limit set by ASTM for 300W/200 mms process parameter [41]. The other elements are well within the permissible range.

Calculated and experimental values of final concentration is listed in

Table v. EDX was used to obtain the final concentration experimentally. When the electron beam hits the sample, x-rays are generated which consist of photons. Silicon/drift detectors are used to measure the energy of these photons. Data generated this way consist of spectra with peaks corresponding to different elements. The heights of the peaks resemble the concentration of each element. The measured intensity of each element of the sample is affected by the composition of the whole sample. Area mapping was conducted on different regions of the sample and the average value was taken.

Table v: Comparison Between Experimental and Calculated Concentration

Elements	Initial Concentration (%)	Experimental Concentration (%)	Calculated Concentration (%)	Error in final concentration (%)
Al	0.55	0.7702	0.4905	36.3063

Cr	18.81	19.3141	18.584	3.7777
Fe	17.7515	18.893	17.8515	5.5146
Ni	53.39	51.102	53.1928	-4.0915
Mo	3.04	3.4133	3.1679	7.1870
Ti	1.02	1.0433	1.03235	1.0570
Nb	5.21	4.922	5.48029	-11.3427

The calculated and experimental values of the final concentrations provided reasonable agreement except Aluminum. EDS does not provide a good analysis of elements with low atomic number, so the inaccuracy with Al is reasonable. The errors for the other elements may be subject to several factors. The EDX mapping could be conducted on a wider range of areas to get a better result. Also, the detector could be placed at a different optimum angle with the sample to obtain accurate peaks from the sample. For the analytical calculation, a different value of $\beta = .05 - .2$ could have offered better outcome as the Langmuir equation over predicts the vapor flux by 5-20%.

2.7. Conclusion

Two finite element thermo-fluid model was generated to determine the temperature profile and melt pool geometry of a non-Gaussian beam. A non-Guassian beam model was proposed to model the laser-material interaction accurately. Temperature profile obtained with the thermal model showed that the maximum temperature was lower for a non-Gaussian beam. Bead geometry was generated from the 2nd model using level set method. Melt pool width and the bead height had a better correlation with non-Gaussian beam than Gaussian beam when compared against experimental values. Elemental evaporation was also determined using the temperature profile obtained from the 3D model. Concentration

change was more significant for alloying elements at higher laser power and lower scan speed. For lower powers and higher scan speed, the change was insignificant. Chromium went through the maximum concentration change due to higher vapor pressure at elevated temperature.

CHAPTER 3

THERMO-PHYSICAL PROPERTIES

This chapter addresses the lack of literary work on experimental data for thermophysical properties by evaluating thermal conductivity, heat capacity and thermal diffusivity of 5 different metallic powders that are commonly used in AM process at elevated temperature. The result is compared to available analytical models. Underlying physics of the thermophysical properties are explained.

3.1. Available Analytical Models for Conductivity

In powder bed fusion process, thermal conductivity of the powders dictates how much of heat is conducted away from the powder bed platform as temperature increases. Thus, it is an important parameter in conducting heat transfer analysis through modeling and simulation. Owing to the complications associated with measuring the conductivity value during AM process, several researchers have attempted to develop analytic models to find out the thermal conductivity of powders. Some of the most well-known models are presented in this section. These models were chosen based on the fact that they have included some parameters like porosity, fluid conductivity, radiation etc. which resembles the events that take place around the powder bed during powder bed fusion AM process.

3.1.1. Hadley

 Hadley [50] modeled the equation as a two-phase system: porous material (Powder) with fluid filled between the gaps.

$$\frac{k_e}{k_f} = (1-a) * \frac{e*f_0+\frac{k_s}{k_f}(1-e*f_0)}{1-e(1-f_0)+\frac{k_s}{k_f}*e*(1-f_0)} + a * \frac{2*\left(\frac{k_s}{k_f}\right)^2*(1-e)+(1+2e)*\left(\frac{k_s}{k_f}\right)}{(2+e)*\frac{k_s}{k_f}+1-n}$$

(19)

Here k_e is the effective conductivity, k_f is the thermal conductivity of the fluid in the build atmosphere, k_s is the solid thermal conductivity, e is the powder porosity, the amount of empty spaces in a bulk material, a and f_0 are the two scaling functions. The value of a depends on degree of consolidation of the powder materials. It is low for loose powders and higher for consolidated powders. So, when the temperature increases, the value of a increases consequently as the powders get consolidated. It was believed that the value of a depends solely upon powder porosity and not on the material itself or particle shape. $f_0 = 0.8 + 0.1 * e$ is another scaling function that is dependent on powder porosity. f_0 was assumed to have a value of 0.84 for the current study.

3.1.2 Sih and Barlow

Sih and Barlow [48] proposed the following equation which has 3 different parts: Heat transfer due to free fluid, Incomplete contact of solid and complete solid contact.

$$\frac{k_e}{k_f} = (1-\sqrt{1-e})\left(1+\frac{e*k_r}{k_f}\right) + (\sqrt{1-e})\left[(1-\emptyset)*\left(\frac{2}{\left(1-\frac{B*k_f}{k_s}\right)}\left(\frac{B}{\left(1-\frac{B*k_f}{k_s}\right)^2}*\left(1-\frac{B*k_f}{k_s}\right)\ln\left(\frac{k_s}{B*k_f}\right)-\left(\frac{B+1}{2}\right)-\frac{B-1}{\left(1-\frac{B*k_f}{k_s}\right)}\right)+\frac{k_r}{k_f}\right)+\emptyset\frac{k_s}{k_f}\right]$$

(20)

The parameters used in this equation previously not mentioned are: B is the particle deformation parameter, $\emptyset$ is a fraction parameter between two adjacent particles. $\emptyset = 0$ for particles with no contact and 1 for particles with full contact, k_r is the conductivity due to

radiation and assumed to have a significant effect at high temperatures. The value of k_r can be predicted from:

$$k_r = 4F\sigma T^3 x_r \tag{21}$$

Here F is the view factor of the radiation that is emitted from the heated powder bed surface having a value of 1/3 which depends on the shape of the particles. σ =5.67*10^{-8} W/m^2.K^4, x_r is the particle size. The value of B is 1 for sphere particles. $\emptyset = 0$ as the there is no complete contact between two powder particles. Putting these values in equation (3) takes the model into the following form:

$$\frac{k_e}{k_f} = \left(1 - \sqrt{1-e}\right)\left(1 + \frac{e*k_r}{k_f}\right) + \left(\sqrt{1-e}\right) * \left(\frac{2}{1-\frac{k_f}{k_s}}\left(\frac{1}{1-\frac{k_f}{k_s}}\ln\left(\frac{k_s}{k_f}\right) - 1\right) + \frac{k_r}{k_f}\right) \tag{22}$$

3.1.3. Yagi-Kuni

Yagi and Kuni [104] considered conduction between the powder particles, convective heat transfer between solid-fluid-solid interface and ion in their model. The equation is as follows:

$$K_e = \frac{\beta*\mu*K_s}{1+\varphi*(K_s/K_f)} \tag{23}$$

Here, β is the ratio of the distance between the center of powder particles, l_p and average powder particle diameter, d_p. $\beta = \frac{l_p}{d_p}$. The value of β typically ranges from 0.82-1 for different packing orientations. β was taken as 1 similar to Bugeda et al [105] in his model of laser sintering process. μ is the ratio between powder density and solid density, φ is an empirical coefficient related to particles void fraction, $\emptyset = 0.02 * 10^{2(0.7-\mu)}$.

Among all the models, the equations provided by Sih and Barlow [48] look more comprehensive as it considers not only the heat transfer of the fluid between particles, but

also radiation, which can play a vital role at higher temperature for porous materials having porosity greater than 0.2, [106] and fraction of contact two adjacent particles are in. Both Yagi and Hadley's models fail to incorporate radiation heat transfer in their models. Also, Hadley's model relies heavily on scaling functions that can incorporate errors.

3.2. Experimental Procedure

All the powders that were selected for this study are generally used in AM process. The powders used for the experiments were made from gas atomization process. In this process, a stream of molten metals is disintegrated by incoming high-speed jet of gas. The droplets subsequently cool down and solidify to powder particle. The size of the powder particles ranged from 45-105 µm at room temperature. The mass and the volume of the powder was measured, with porosity being 0.4. The composition of the powder alloys is given in the following table:

Table vi: Powder Composition

Inconel 718		Ti6Al4v		SS 316L		SS 304L		CoCrMo	
Element	Weight(%)	Element	Weight(%)	Element	Weight(%)	Element	Weight(%)	Element	Weight(%)
Ni	52.95	Ti	89.63	Cr	17.57	Cr	19.38	Cr	27.7
Nb	5.33	V	3.99	Mo	2.6	Ni	9.84	O	0.0113
Mo	3.13	Fe	0.2	Ni	11.32	Mo	0.78	Mn	5.8
Cr	18.96	Al	6.1	Mn	0.53	Mn	0.11	N	0.0075
Al	0.41	O	0.0785	Si	0.96	Si	0.042	Co	Balance

Other	<0.1	H	0.0012	Others	<0.1	Others	<0.1		
s									
Fe	Balance	N	0.0028	Fe	Balance	Fe	Balance		

3.3. Heat Capacity

A commercial Differential scanning calorimeter, DSC 25 (TA instruments, USA) was used to carry out the specific heat experiment. This instrument can detect specific heat of solid, liquid, powder up to 725^0 Celsius [107]. The sample cells were calibrated with indium (In) before the experiment. Then the specific heat of sapphire was measured. Sapphire has well established value of specific heat capacity up to 1000^0 C. Afterwards, the heat capacity calibration constant, K (C_p), was calculated which is the ratio of the theoretical to the measured heat capacity of sapphire.

$$k\left(C_p\right) = \frac{C_{p.theoretical}}{C_{p.measured}} \tag{24}$$

This calibration constant was multiplied by the measured heat capacity of the powders to get the actual value. Alumina pans were used, which have high melting temperature. The pans are extremely flat and thus improves the contact with sensors and therefore enables good heat flow signal collections from the sample, which ensures improved resolution and sensitivity. Nitrogen was used as purge gas and a finned air-cooling system was used (FACS) to cool down the system. There are two pans inside the cell; one of them is empty (Reference pan), the other carried the powder sample. Around 10 mg of powder sample was inserted into the pan. A lid was placed upon the pan and tightened using a press. The difference of temperature between the reference pan and sample was recorded with time to determine the heat flow. Then heat capacity is measured using the following formula:

$$C_p = \left(\frac{\frac{dH}{dt}}{\frac{dT}{dt}}\right) * k \qquad (25)$$

Here, C_p is the specific heat capacity in J/Kg. K, dH/dt is the heat flow in W/kg and dT/dt is the heat rate in K/s.

Heat capacity was calculated by TRIOS software two times: one during heating and the other during cooling. Modulated Quasi isothermal mode was used where temperature was kept constant for 30 minutes at desired temperatures to get accurate data.
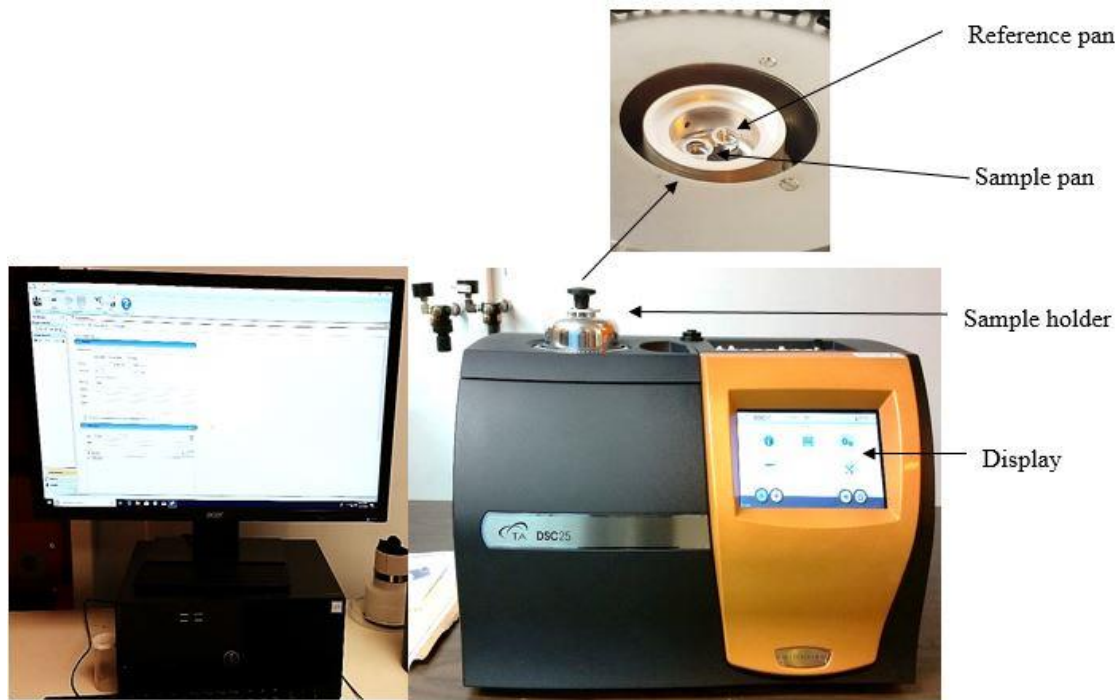

Figure 10: DSC Setup

3.4. Thermal Diffusivity and Conductivity

Current technology does not allow measurement of thermal conductivity directly accurately. However, an indirect method utilizes a thermal diffusivity and thermal capacity to extract thermal conductivity as follows: [108]

$$\alpha = \frac{k}{\rho . C_p} \tag{26}$$

Here, α is thermal diffusivity in m^2/s, k is thermal conductivity in W/m.K, ρ is density in Kg/m^3, C_p is heat capacity in J/Kg.K.

Heat diffusivity was measured using DXF-900 instrument [109]. It can measure temperature up to 900^0 Celsius with an accuracy of 2.3%. Thermal diffusivity is defined as how fast heat can transfer from hot temperature region to cold region. Diffusivity measurement is based on the flash method. Laser flash technique is one of the most efficient means to measure diffusivity over a range of elevated temperature. This transient technique is a definite test in the way that it does requires little to no calibration, features short measurement times, is completely non-destructive, and delivers result with exceptional accuracy and duplicability. A xenon or laser heat source irradiates the top of the sample uniformly. The temperature rise in the top face creates a thermal gradient with the opposite face, which propagates heat to the rear end. A temperature detector records the time dependent temperature history of the opposite face of the sample of the opposite face of the sample in a short period of time. Thermal diffusivity is then calculated using the thickness of the sample (L) and time it takes to reach half of the maximum temperature rise $(t_{1/2})$ using the following equation:

$$\alpha = 0.1388 \times \frac{L^2}{t_{1/2}} \tag{27}$$

This method was originally developed by Parker et al. [110]. This model assumes constant temperature and adiabatic condition with no heat loss, both of which can incorporate errors. These assumptions are corrected in the present technique to acquire better result. The powders were placed on the sample holder up to a height of 0.1063 cm and closed with a

lid. Both the lid and the holder were coated with graphite spray, so the laser power does not get scattered and all the power is absorbed for better accuracy.
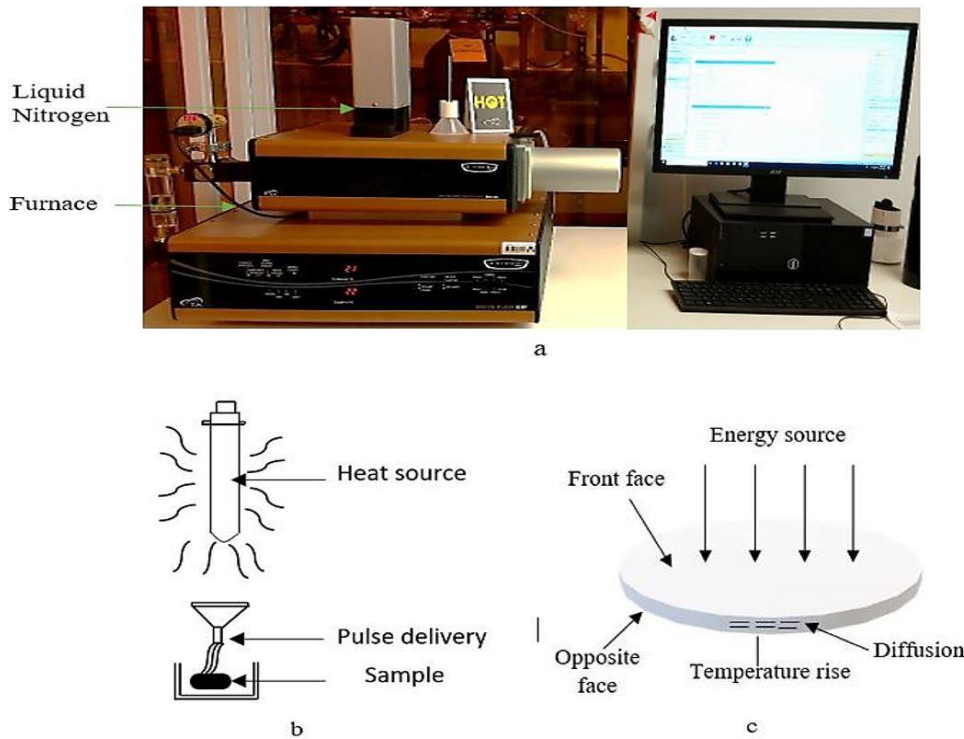
Figure 11: (a) DXF 900 Setup (b) Flash Configuration (c) Diffusion Technique

3.5. Result and Discussion

3.5.1. Heat Capacity

Specific heat capacity of 5 different powders: Inconel 718, Ti6Al4V, SS 316L, SS 304L and CoCrMo are depicted in **Figure 12** from 323K-873K temperature. Error bars were calculated based on uncertainty measurements from 3 readings at each temperature point using Student's t-distribution method for 95% confidence interval. Most of the thermal models assume the heat capacity of a metallic powder to be equal to the heat capacity of the bulk material [31] [111]. But there are some gases entrapped in between the powder particles. Although the heat capacity of the gases is large, their low density makes their

49

overall contribution to the heat capacity to the whole matrix insignificant. Regardless, we compared our experimental data with the analytical model of Zhang et al [112] who considered heat capacity of air to their model. The heat capacity equation is given by [112]:

$$C_{p.powder} = \frac{\rho_s * \eta * C_{p.s} + \rho_g * (1-\eta) * C_{p.g}}{\rho_s * \eta + \rho_g * (1-\eta)} \tag{28}$$

Here, ρ_s and ρ_g are the density of the solid and gas, η is the powder packing efficiency, $C_{p.s}$ and $C_{p.g}$ are the heat capacity of the solid and gas respectively.

Figure 12 shows that all measured thermal capacity follows a nonmonotonic trend with dipping at higher temperatures. Analytical models fail to show this non-monotonic trend, except in Inconel 718. Owing to its lower density and higher thermal capacity of solid, Ti6Al4v has the highest heat capacity among the powders. Both Inconel 718 and Ti6Al4v produce contrasting peak at around 773K and 873K temperature absorbing (endothermic) and releasing (exothermic) heat respectively [66]. Enough information of CoCrMo could not be obtained to calculate its heat capacity from theoretical model. It experiences decline in heat capacity at around 550K and 750K.

The difference between the chemical composition of SS 304L and SS 316L is the inclusion of 2-3% molybdenum to SS 316L to improve corrosion resistance [113], [114]. This somewhat increases the density of SS 316L compared to SS 304L. It may be one of the reasons that the heat capacity of SS 304L is more than SS 316L. Kim [115] proposed two separate equations of heat capacity for SS 316L and SS 304L that linearly increases with temperature. Kim's models are used exclusively for SS 316L and SS 304L.

$$\text{SS 304L: } C_p = 0.1122 + 3.222 \times 10^{-5} T \tag{29}$$

$$\text{SS 316L: } C_p = 0.1097 + 3.174 \times 10^{-5} T \tag{30}$$

Here, C_p is the heat capacity in cal/(g). (K) and T is the temperature in K. Both models

slightly overpredict the heat capacity values of the powders.
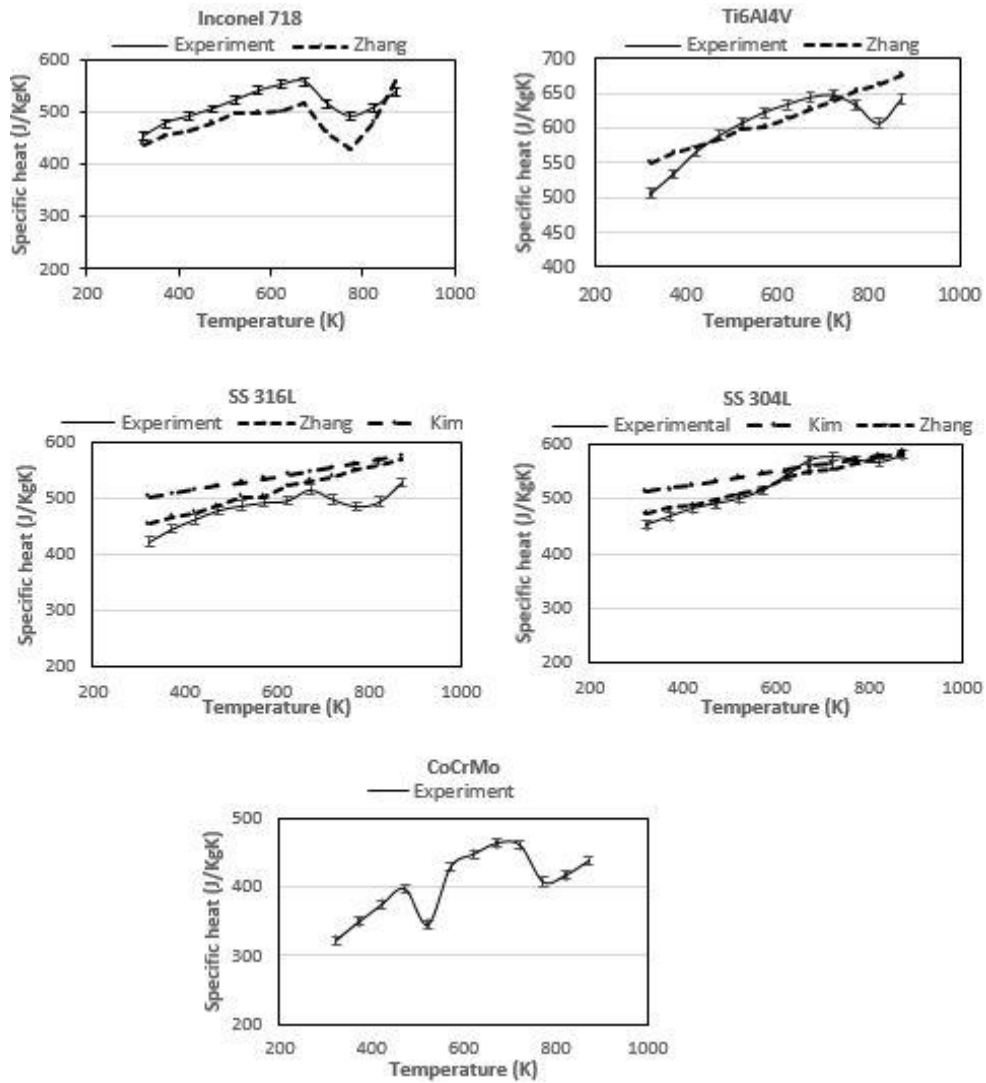
Figure 12: Specific Heat Capacity of (a) Inconel 718, (b) Ti6Al4v, (c) SS 316L, (d) SS 304L, (e) CoCrMo Experimentally Measured and Compared Against Available Models in Literature

3.5.2 Thermal Diffusivity

Thermal diffusivity obtained from the flash technique is given in **Figure *13***. The measurements mostly show varying rate and non-monotonic trend with respect to temperature. Initially, diffusivity decreases, but starts to increase at higher temperature points. This is most possibly due to the fact that at higher temperature, the contact area between particles increases due to initiation of sintering. As a result, the heat is diffused rapidly at higher temperature points through the contact points. Ti6Al4v had the highest diffusivity among the alloys, which could be attributed to the fact that solid Ti6Al4v has higher diffusivity value than the other alloys [116] [117] [118] [76]. The value was also similar to result obtained by Arce et al [119]. Error bars were drawn for 3 laser shots taken at each temperature point.
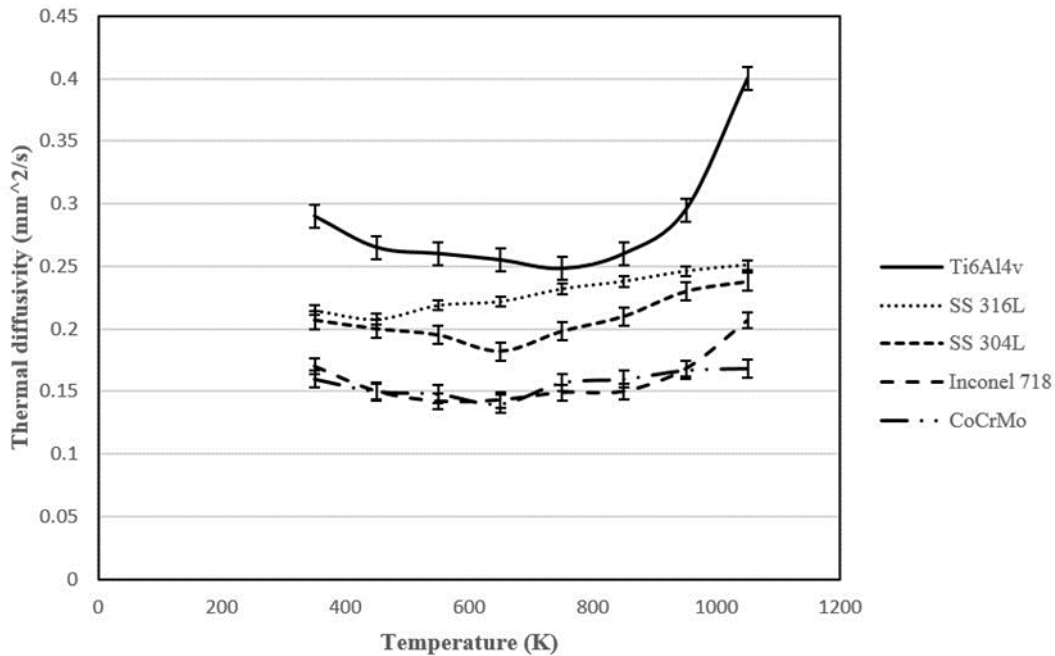
Figure 13: Thermal Diffusivity for Different Powders

3.5.3. Thermal Conductivity

Figure 14 represents the temperature dependent thermal conductivity values and comparison with analytical models developed by Sih et al[48], Hadley et al [50] and Yagi et al [104] for the alloy powders. As the thermal conductivity values were calculated from an analytical formula, uncertainty was propagated based on the uncertainty of heat capacity and thermal diffusivity measurements using the following equation:

$$U_k = \sqrt{(\frac{\partial k}{\partial C_p} * U_{C_p})^2 + (\frac{\partial k}{\partial \alpha} * U_\alpha)^2} \tag{31}$$

Here,U_k, U_{C_p} and U_α are the uncertainties in conductivity, heat capacity and diffusivity respectively.

The model of Agapiou [51] was not used as it represents the conductivity of sintered powders. All the analytical models overpredict the value of thermal conductivity. However, model presented by Sih and Barlow [48] predicts the thermal conductivity most accurately as it is the most comprehensive model, while the other two models overpredict the values. Like heat capacity, these models fail to capture the non-monotonic behavior in conductivity value with temperature.

Figure 14a shows that for Inconel 718, thermal conductivity initially decreases with temperature and reaches a minimum at 600-800 K temperature. Nickel is the main constituent of Inconel 718 that consists 50-55% of the total composition. It is a ferromagnetic material having curie temperature of 627K, which also shows a decreasing trend in conductivity up to the curie point and then starts increasing [120]. This describes the behavior of Inconel 718. Beyond 800 K, the conductivity graph shows a steep rise.

53

Conductivity of Ti6Al4v is lower compared to the other powders due to its lower density. Ti6Al4v starts sintering at 700^0 Celsius [121]. The contact area of the sintered powders is greater than contact area of loose powders. As a result, there is a sharp rise in conductivity after 700^0 Celsius.

SS 304L and SS 316L show similar trend in thermal conductivity values with increasing temperature. Conductivity mostly increases with temperature. Sih and Barlow model [48] can predict the trend within 10% accuracy.

Thermal conductivity of CoCrMo takes a dip at around 700 K and then increases linearly with temperature. It was not compared with analytical models as thermal conductivity value of the bulk CoCrMo could not be obtained from literature which is essential to calculate the conductivity of powder from the analytical models.
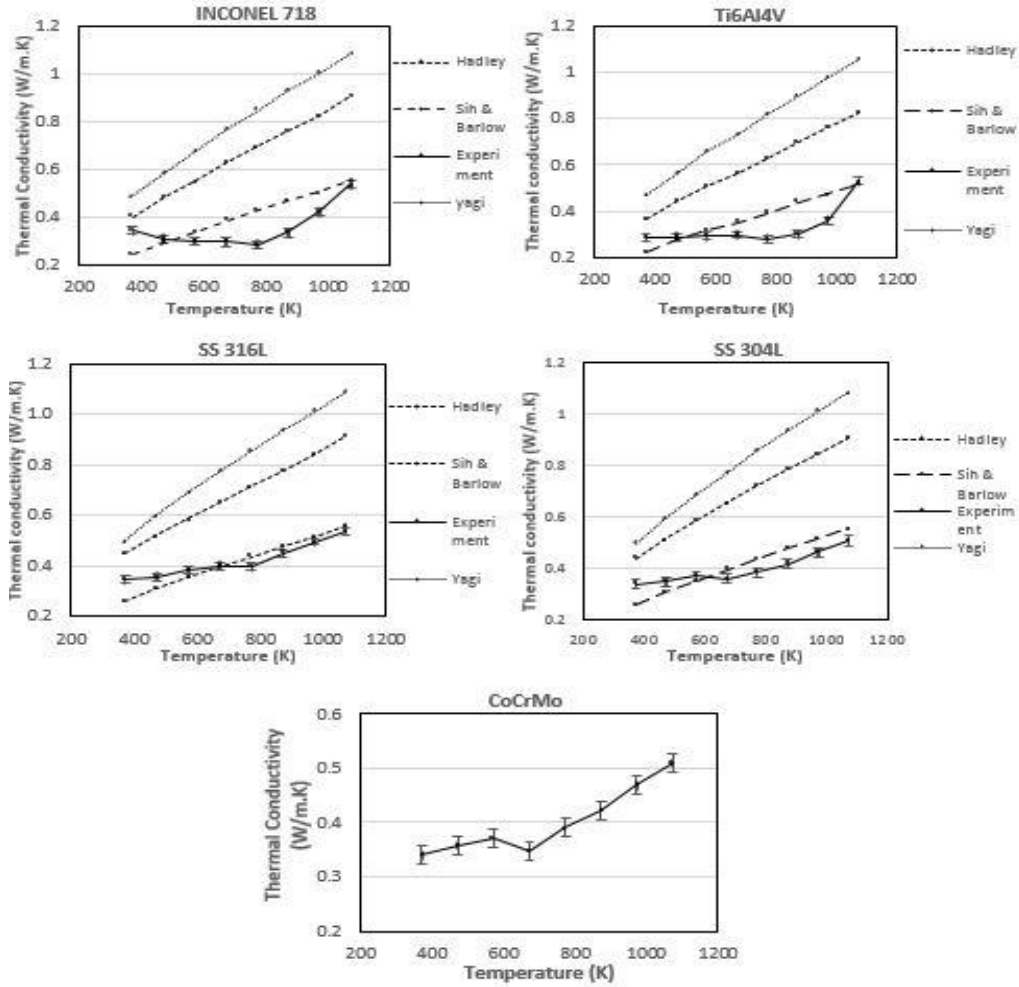
Figure 14*: Thermal Conductivity of (a) Inconel 718, (b) Ti6Al4v, (c) SS 316L, (d) SS 304L, (e) CoCrMo

Thermal conductivity of the powders obtained using the flash technique is very accurate as it considers the loss of heat during the experiment compared to the original Parker's model where adiabatic conditions are assumed [110]. So, it can be inferred that the thermal conductivity values calculated in this study had good accuracy for all the powders used. When thermal conductivity of porous materials are very low (Around 0.1-0.5 W/m.K), it is essential to consider the heat transfer through radiation as well [122]. It can be thus implied that the model provided by Sih and Barlow have performed better than the other models as it took into account of the radiation heat transfer across the pores. It was observed

55

that emissivity plays a key role at temperatures higher than 500^0C [106]. So, the model can be further improved by including emissivity at high temperatures.

Thermal conductivity of solid particles depends on the formation of grain as well as the thermal resistance experienced at the boundaries of the grain. At temperature higher than 20^0C, heat is conducted across the grain by lattice vibration. Heat is also scattered at the boundaries, which hampers lattice vibration. As the size of the grains become smaller, number of grain boundaries increase, which consequently decreases the thermal conductivity [122]. So, incorporating the grain orientation and size will significantly improve the analytical models.

Based on the experimentally found thermal conductivity results, several regression analyses were conducted for each of the powder. It was found that polynomial regression was the best fit for the experimental values. **Table vii** shows the polynomial equations up to 3 orders with R^2 values for each powder.

Table vii: Polynomial Fit Equations for Thermal Conductivity

	Equation	R^2 value
Inconel 718	$10^{-9} * T^3 - 2 * 10^{-6} * T^2 + 0.0006 * T + 0.305$	0.9936
Ti6Al4v	$3 * 10^{-9} * T^3 - 6 * 10^{-6} * T^2 + 0.0039 * T - 0.4453$	0.982
SS 316L	$4 * 10^{-10} * T^3 - 6 * 10^{-7} * T^2 + 0.0004 * T + 0.2469$	0.9223
SS 304L	$5 * 10^{-10} * T^3 - 6 * 10^{-7} * T^2 + 0.0004 * T + 0.27$	0.9866
CoCrMo	$3 * 10^{-10} * T^3 - 3 * 10^{-7} * T^2 + 0.0001 * T + 0.3233$	0.9678

The regression model can capture the higher values of conductivity at elevated temperature due to sintering of the powder particles as well as radiation. These equations may not provide perfectly accurate data, but they will demonstrate an idea how can the thermal conductivity values vary at high temperatures for each of the powders. **Figure 15** shows a comparison of the experimental results against the regression fit analysis.
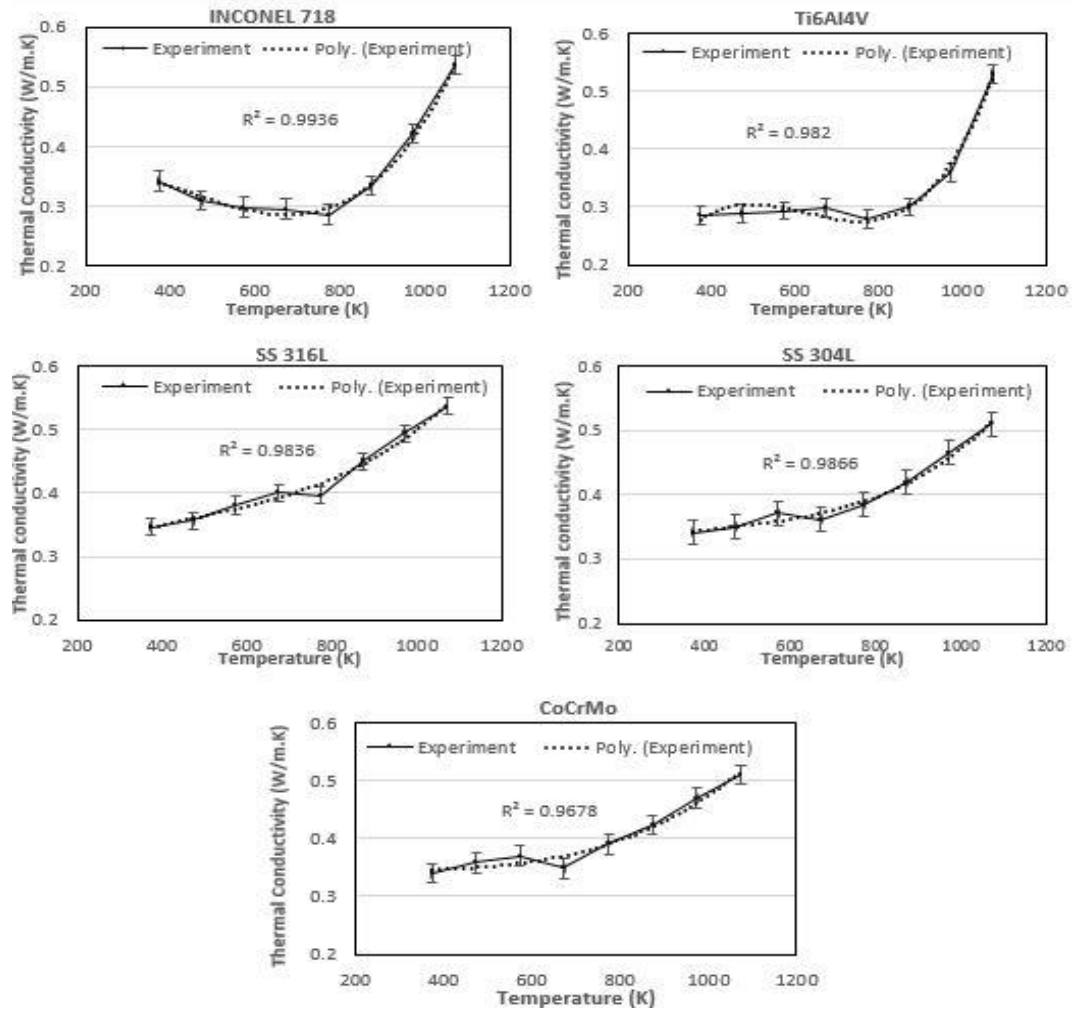
Figure 15: Comparison between experimental result and polynomial fit regression for the powders

3.6. Conclusion:

- Heat transport through metallic powders is essentially dictated by thermal conductivity and heat capacity in transient problems. This work is an attempt to improve the thermal modeling efforts by inputting experimental values of the thermo-physical properties which are essential to obtain desired results.

58

- Thermal conductivity and diffusivity up to 800^0 C and specific heat capacity of up to 600^0 C of 5 common powders used for metal AM were measured and compared against available analytical models.

- Each powder has their own patterns of these properties at elevated temperatures. Generally, they show a non-monotonic behavior for both conductivity and heat capacity. Higher values at high temperatures indicate initiation of sintering, which allows greater heat transfer path between powder particles by increasing contact area.

- The model developed by Sih and Barlow [48] to determine thermal conductivity performed better than the other two models to predict thermal conductivity as the model does a comprehensive analysis of the thermal environment during the process including heat transfer between particles, heat transfer though fluids and radiation effect due to high temperature. The issue with the analytical models is they are not able to predict the decreasing trend of these properties with increasing temperature.

- Regression analyses was conducted for the conductivity of the powders. Polynomial fit performed well with high R^2 values for each of the powder.

UPDATED MULTIPHYSICS MODEL

This chapter uses experimentally obtained thermophysical properties that were obtained in chapter 2, as well as some updated boundary conditions to improve the previous model. The nature of the fluid flow under the effect of surface tension, marangoni convection, recoil pressure, and buoyancy force are explained in this section. A dimensional analysis is also conducted to assess the importance of convective heat transfer through melt pool.

4.1. Boundary Conditions

The top surface of the model was exposed to radiation and natural convection with the atmosphere. Symmetry at y direction was used to save computational time [31].
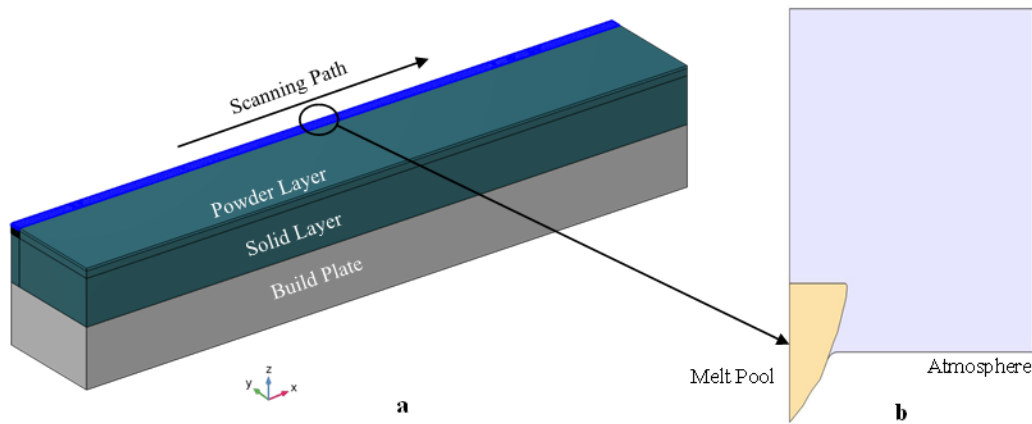
Figure 16: a) 3D Model setup b) 2D Melt Pool Extracted from the 3D model

The temperature gradient created during the process due to localized heating develop surface tension gradient on the powder bed surface. This gradient leads to Marangoni force, pulling fluid away from the hot region. This force acts as a normal component of the shear stress on the free surface of the fluid. This force is modeled with navier-stokes equation [96]:

$$\left[-pI + \mu(\nabla u + (\nabla u)^T - \frac{2}{3}\mu(\nabla.u)I) \right] n = \gamma \nabla_t T \tag{31}$$

Here, p is the pressure, u is the velocity field, μ is the dynamic viscosity, γ is the Temperature derivative of surface tension.

Non-isothermal condition was applied in the whole domain where fluid properties like density, viscosity etc. are temperature dependent [123]:

$$-n.q = \rho C_p^{1/4} k^{1/2} \frac{T_w - T}{T_{amb}} \tag{32}$$

Here, q is the heat flux, ρ is the density, Cp is the heat capacity, T_w is initial surface temperature, T_{amb} is the ambient temperature and k is the thermal conductivity.

Recoil Pressure was used on the surface only when the temperature exceeded the vaporization temperature of Inconel 718:

$$P_{recoil} = \frac{0.54 \times P}{1} \times exp\left(\frac{H_v \times (T - T_{ev})}{R \times T \times T_{ev}} \right) \tag{33}$$

Here, H_v is the enthalpy of vaporization, T_{ev} is the vaporization temperature and R is the universal gas constant.

4.2. Material Properties

To fill the gap of experimentally obtained data for thermophysical properties of Inconel 718, thermal diffusivity was measured using a DLF 1600 instrument up to 1400 C, and heat capacity was measured using DSC 25 up to 625 C. Thermal conductivity was calculated using the following equation:

Thermal conductivity, $k = \alpha \times \rho \times C_p$ \hfill (34)

Here, α= Diffusivity, ρ= Density, C_p = Heat capacity
A detailed analysis of the experiments can be found in our previous work [78].
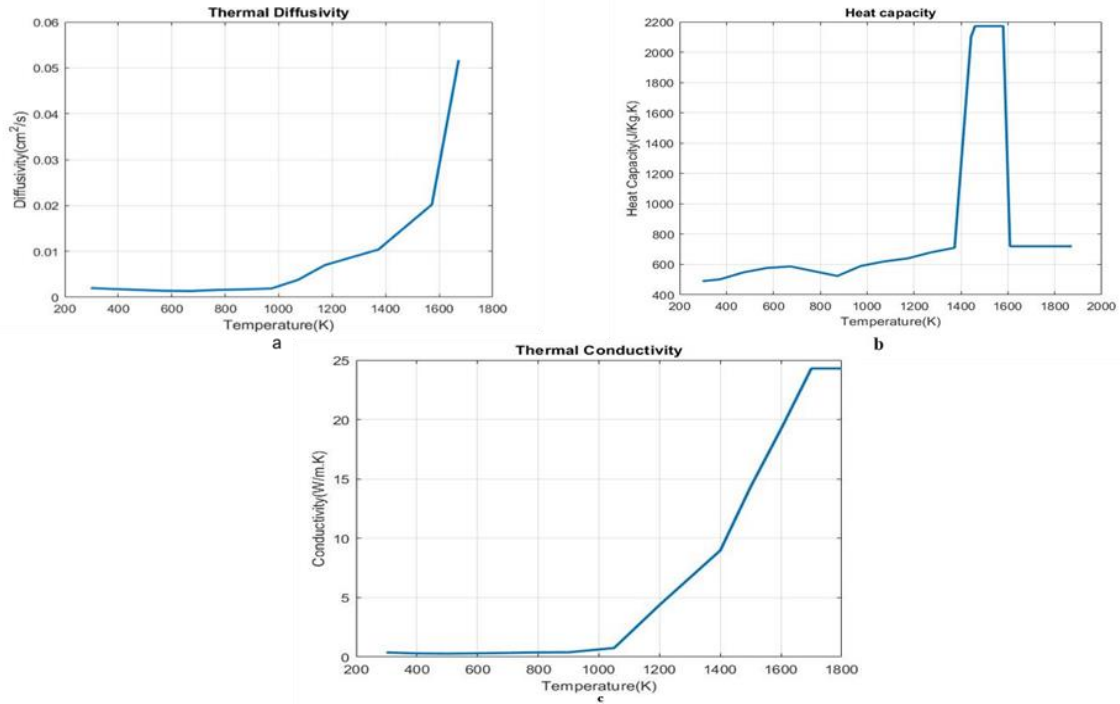
Figure 18: a) Thermal diffusivity, b) Heat capacity c) Thermal conductivity of Inconel 718 measured experimentally at elevated temperature.

Other material properties like density, dynamic viscosity was imported from literature.
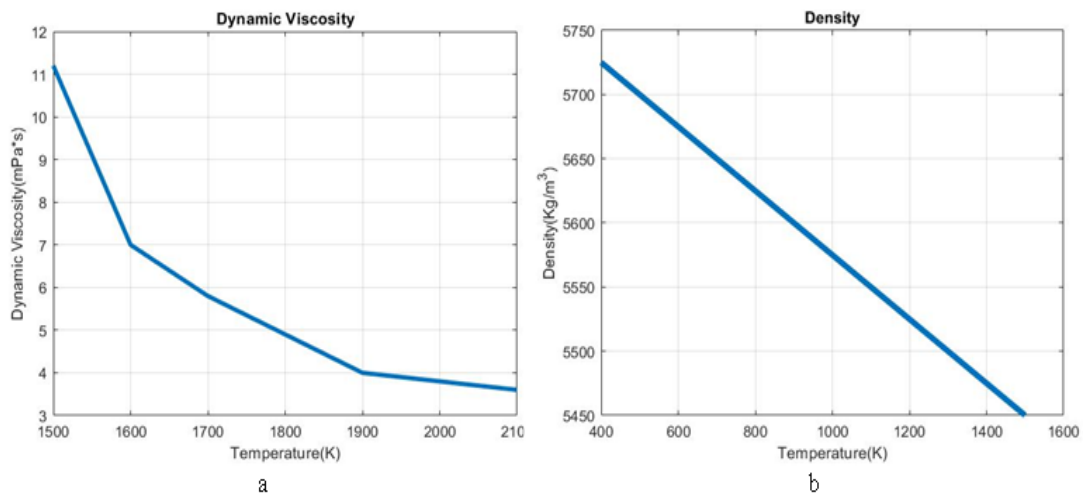
Figure 19: a) Dynamic viscosity b) Density of Inconel 718

4.3. Dimensionless Numbers

In this paper, dimensional analysis was conducted to evaluate the effect of various mode of heat transport such as conduction and convection, their relative importance in the evaluation of molten pool and the parameters that can impact these processes.

Nusselt Number: Nusselt number [124] is defined as a ratio between convective and conductive heat transfer. Nusselt number was calculated using the following process:

Internal Energy, $E = H - p/rho$

Convective Heat Flux, $Q_{conv} = \rho * u * E$

Convective heat transfer coefficient, $h = \dfrac{Q_{conv}}{T_{max} - T_s}$

Nusselt Number, $Nu = \dfrac{h * l_{ch}}{k}$ (35)

Here, l_{ch}=Melt pool characteristic length, ρ= Density, H=Enthalpy, p= Absolute pressure

Peclet Number: Peclet number is the product of Reynolds and Prandtl number. Higher Peclet number signifies higher momentum transfer and flow rate as Reynolds No is a measure of flow rate and prandtl no. It is the ratio of kinematic viscosity (measure of momentum transfer) to heat diffusivity (measure of heat transfer).

Peclet Number [125], $Pe = Re * Pr = \dfrac{u * l_{ch}}{\alpha}$ (36)

Here, Re= Reynolds number, Pr= Prandtl number, l_{ch}=Characteristic length of the melt pool, which is taken as the length of the melt pool consistent with work done by Mukherjee et al.[76], u= maximum velocity within the melt pool to account for the highest peclet number around that region.

The dimensionless numbers are summarized in the following table.

Table viii: Dimensionless Numbers

Dimensionless Number	Equation
Nusselt Number	$Nu = \dfrac{h * l_{ch}}{k}$
Peclet Number	$Pe = \dfrac{u * l_{ch}}{\alpha}$

4.4. Results:

4.4.1 Temperature Profile

Temperature contour and profile along the scanning direction is shown in *Figure 20* at a specific time. Temperature is highest at the center of the beam owing to the maximum intensity at that point, then decays exponentially as it moves outward. As the beam has been modelled to follow a realistic pattern, it deviates slightly from an ideal or Gaussian beam. A comparison has also been drawn with our previous model [31]. The updated model has used experimental thermophysical properties at elevated temperature. We have also balanced the marangoni force with navier stokes equation whereas the force was modelled as a weak expression in the previous model. This model includes recoil pressure as well that was missing from the previous one. As observed from figure *Figure 20b*, incorporating experimental material properties and recoil pressure has changed minimized the highest temperature by a margin of about 290K. As the material temperature exceeds its vaporization temperature, the temperature decreases as energy is lost during vaporization process. The temperature profile has also turned wider as the gradient in surface tension

has caused the liquid to flow from high to low temperature region and carry some heat with it.
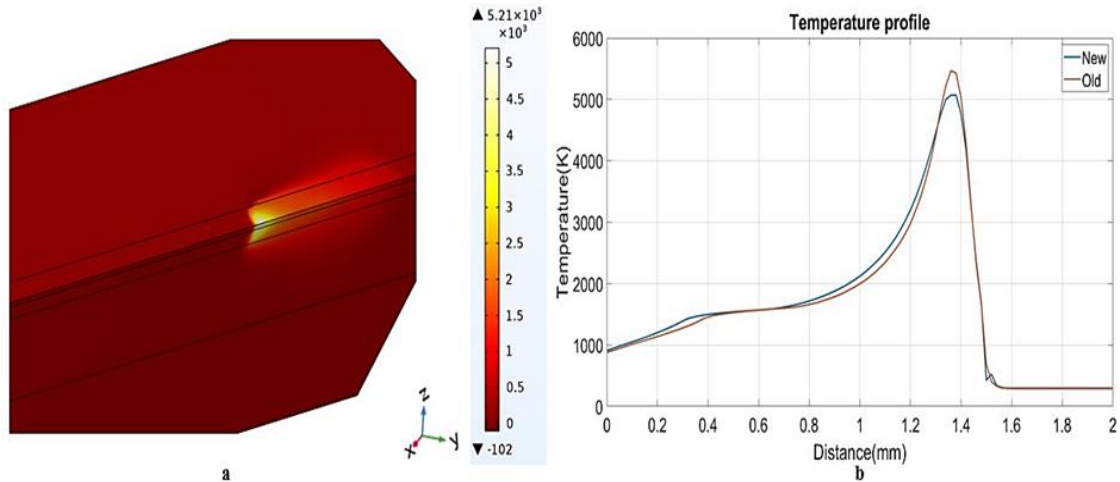
Figure 20: a) Temperature contour b) Temperature profile for new and old models at t=0.0067s for laser power = 300W and scan speed = 200 mm/s

4.4.2. Velocity Profile

Figure 21a shows the fluid velocity contour at the X-Y plane on the top surface at z=0. The value of the fluid speed varies from 0.2 to 0.34 mm/s, where the temperature exceeds the melting point of Inconel 718. At the center of the melt pool where temperature is maximum, velocity is low and increases towards both side of that point. This can be seen in *Figure 21b*, where a plot is drawn along x axis, which is the scanning direction. There are 2 peaks on either side of the melt pool, among which the maximum velocity is achieved after the laser scanning point. This is due to the fact that surface tension forces are higher at high temperature gradient, propelling the fluid towards that direction at a higher speed. On the other hand, t peak has already been scanned, making that zone in a higher temperature region, making the flow of fluid lower. The same fact drives curve wider. The -y direction velocity is higher at the middle, along the radius of the melt pool. As we go

65

further, the effect of surface tension diminishes, and no considerable velocity of fluid is visible.
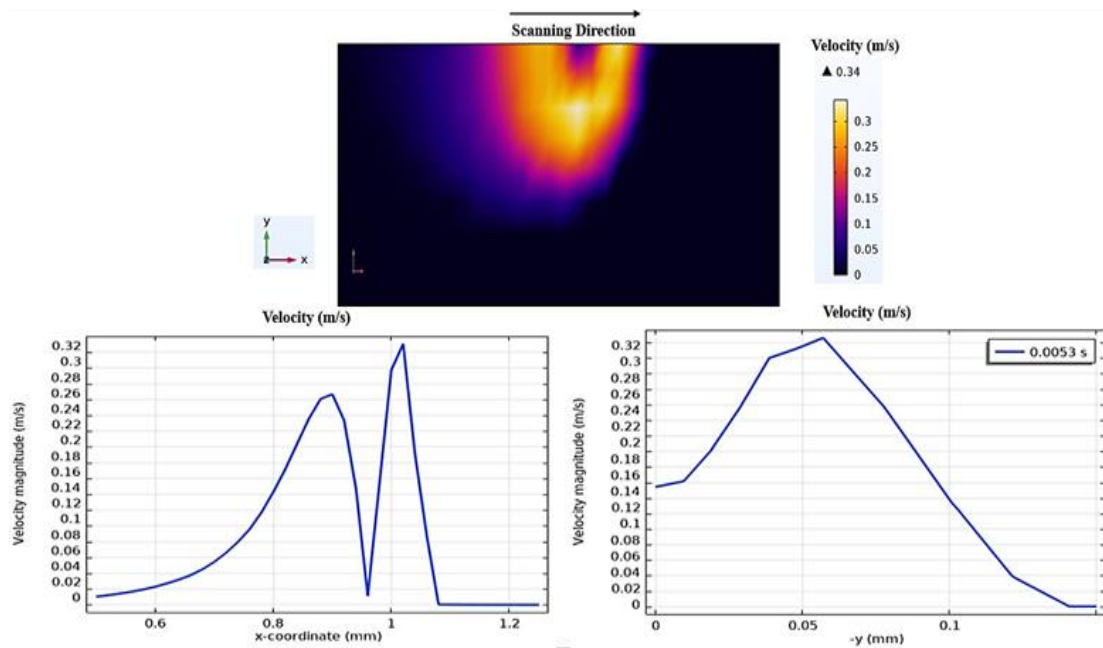
Figure 21: a) Velocity contour at the top surface b) Velocity profile at the scanning direction (x axis) c) Velocity profile along -y direction for laser power = 300W and scan speed = 200 mm/s

4.4.3. Melt Pool Flow

Flow inside the melt pool is also shown *Figure 22* in along with the temperature contour to have a better understanding of the nature of the flow. The vector field is captured at a specific time. In *Figure 22c* along the depth, there are two vortexes, one clockwise before the center of the beam, and one after the center of the beam having a counterclockwise direction. Around the top surface, the velocity is much higher because of the high surface tension gradient around the highest temperature region which is indicated by the thicker arrow lines. As we go deeper along the depth, velocity starts decreasing. Maximum velocity was found to 0.34 m/s, whereas minimum value was 0.11 m/s around the melt pool. Larger velocity indicates high convection heat transfer along the radius of the beam.

Buoyancy also affects the melt pool. As the temperature is lower beneath the surface, the density of the material increases, which pushes the fluid upwards to the center of the molten pool. The comparative effect of buoyancy and surface tension driven flow can also be assessed from a parameter called bond number, which is the ratio between density driven flow by surface tension driven marangoni flow [126]:

$$Bo = \frac{\Delta\rho * g * w}{d\gamma/dT}$$

Here, $\Delta\rho$ is the change in density, w is the width of the melt pool, g is the gravitational acceleration, and $d\gamma/dT$ is temperature gradient of surface tension. The value of bond number was $50 * 10^{-3}$ for a laser power and scan speed of 300W/200 mm/s, which is extremely low, indicating the impact of significant marangoni flow, compared to the buoyancy driven flow. Bond number was low for other process combinations as well.

From *Figure 22b,* direction of marangoni flow is evident on the top surface. Fluid streams from the center to the edge of the laser beam, thus forming a melt pool. A cross section of the YZ plane *(Figure 22b)* shows how the development of velocity helps to create a melt pool when the laser scans a particular point at a specific time under surface tension and gravity.
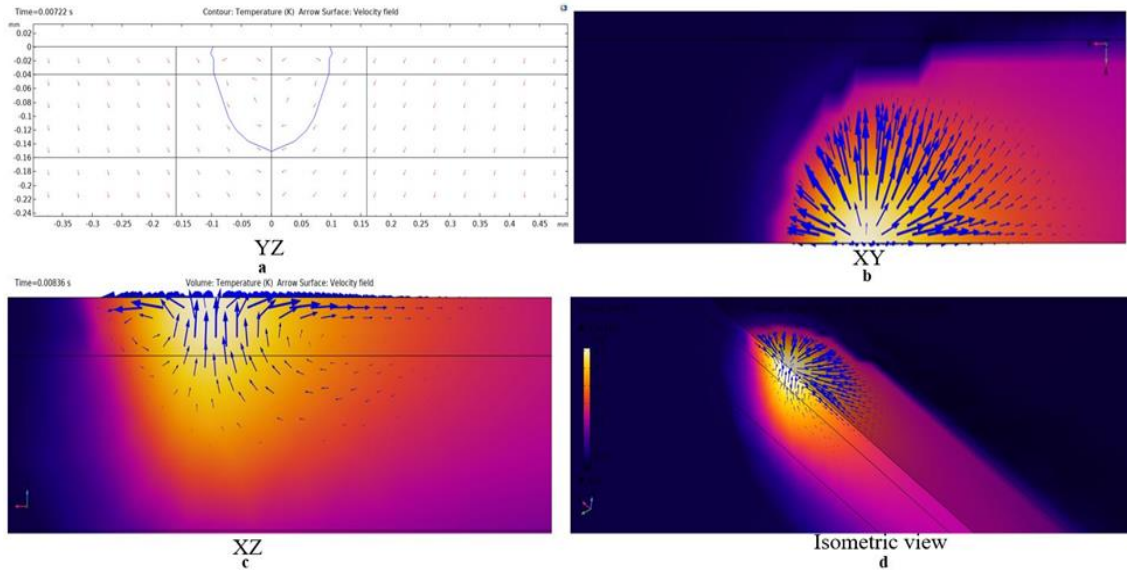
Figure 22: Fluid flow arrow lines with temperature contour a) YZ plane b) XY Plane c) XZ Plane d) Isometric view

4.4.4. Model Validation

Experimental result from Sadowski et al. [5] from our group was used to compare the updated model against the previous one. For various laser powers ranging from 100W to 300W at a scan speed of 200 mm/s, the results for melt pool width and depth are showed in Figure 23. As expected, both width and depth increase significantly with higher power because of the greater energy input. Updated marangoni force has improved the melt pool width significantly with the result being close to experimental values. Using recoil pressure to depress the melt pool at higher laser powers has also proved to be useful as the simulation result follow the experimental trend well. Melt pool depth was significantly higher than the layer thickness for higher power, indicating laser could penetrate through the substrate for initial layers.
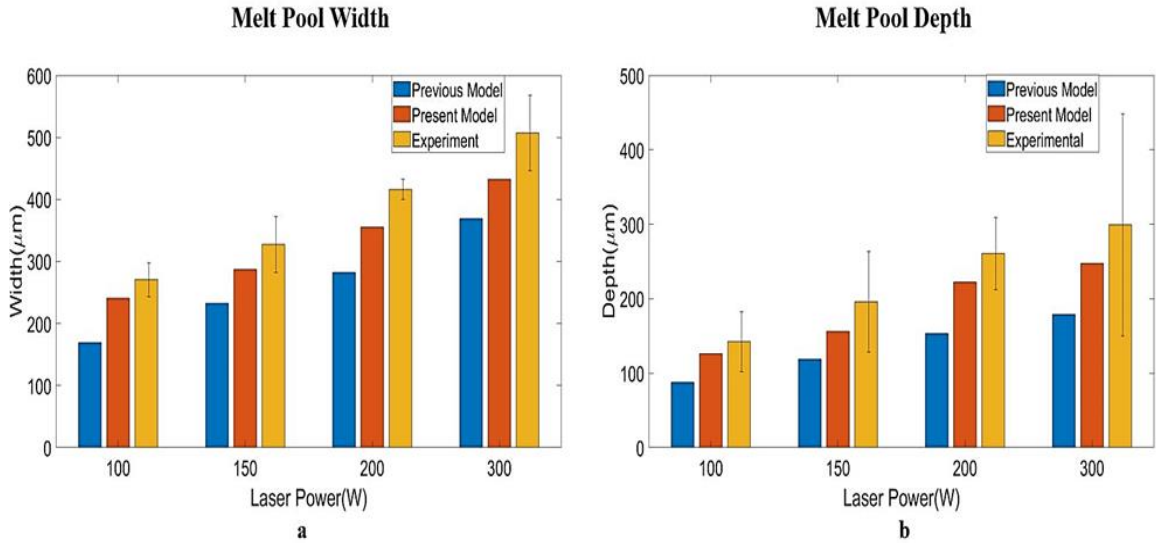
Figure 23: a) Melt Pool Width b) Melt Pool Depth Comparison Against Previous

Simulation and Experimental Results

4.4.5. Dimensional Analysis

Figure 24a shows the convective heat transfer coefficient when the laser passes the selected region for a combination of 300 W/200 mm/s process combination. As the laser heating is highly concentrated, melting occurs over a small region of the powder bed, creating a rapid flow of fluid around that region, that results in a high value of heat transfer coefficient. The h value was compatible with value found by Romano et al (3.79*106 W/m2.K) [1]. The difference in the result could arise from the fact that they used an effective conductivity value instead of modeling fluid flow, which could induce some errors. ***Figure* 24b** shows the variation of Nusselt number along the laser scanning direction at a specific time for 300W/200mms-1 combination. Nusselt number is low initially and start getting high when the powders get heated. Nu has two peaks and highest just after the scanning point, suggesting it is mainly driven by the convective flow of fluid within the melt pool. ***Figure* 24c** demonstrates the Peclet number which shows similar pattern as the Nusselt number. Higher peclet number indicates that momentum transfer is the more prominent feature compared to diffusion. Inconel 718 has a relatively lower thermal diffusivity, resulting in higher peclet number. Although exact comparisons were not possible due to the variability of process parameters, result was consistent with the values found by Mukherjee et al [76].

Figure 25 represents the variation of Nusselt and Peclet number as a function of marangoni number which is increasing with laser power input. As the marangoni number increases, both peclet and Nusselt number increase and significant amount of heat is transferred by convection. At smaller Pe and Nu numbers, convection is not significant, and conduction

is the more dominant form of heat transport. As the Marangoni number increases, the fluid

within the melt pool becomes more violent with increasing velocity, which induces

convection. Peclet and Nusselt number higher than 20 [76] indicates that the momentum

due to fluid velocity get increasingly dominant, which can even create pores and other

defects within the melt pool that can be observed from experimentally obtained bead

geometry. Generation of recoil pressure due to high process temperature along with larger

melt pool area can depress the surface that can create keyhole along z axis of the melt pool

[127]. The fluctuation in the met pool due to keyhole formation can trap the metal vapor

within the keyholes that can create defects like porosities [128].
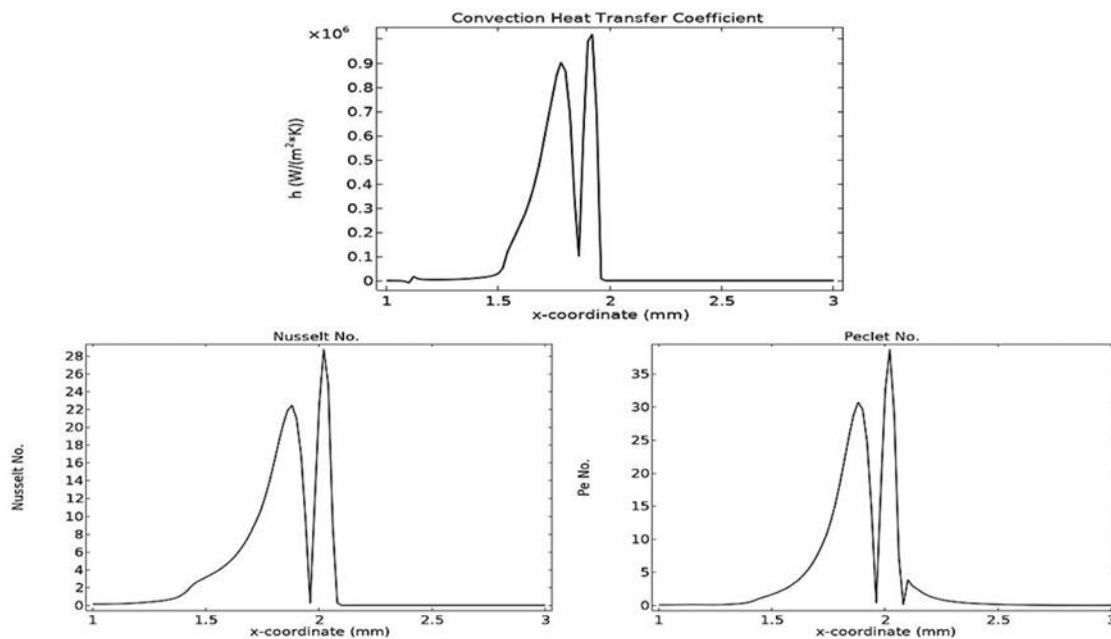
Figure 24: a) Convection heat transfer coefficient b) Nusselt Number and b) Peclet
Number as a Function of Position for 300W/200mm/s

Figure 25 links high values of Peclet and Nusselt number that leads to such defects at

higher energy input (Process parameters of 300W/200mm/s). The keyhole dynamics is a

complex phenomenon which can arise due to a number of reasons. High Peclet and Nusselt

71

number indicate instability in the melt pool which is one of the most dominant mechanisms behind this phenomenon. This can be better explained by constructing a turbulence model.
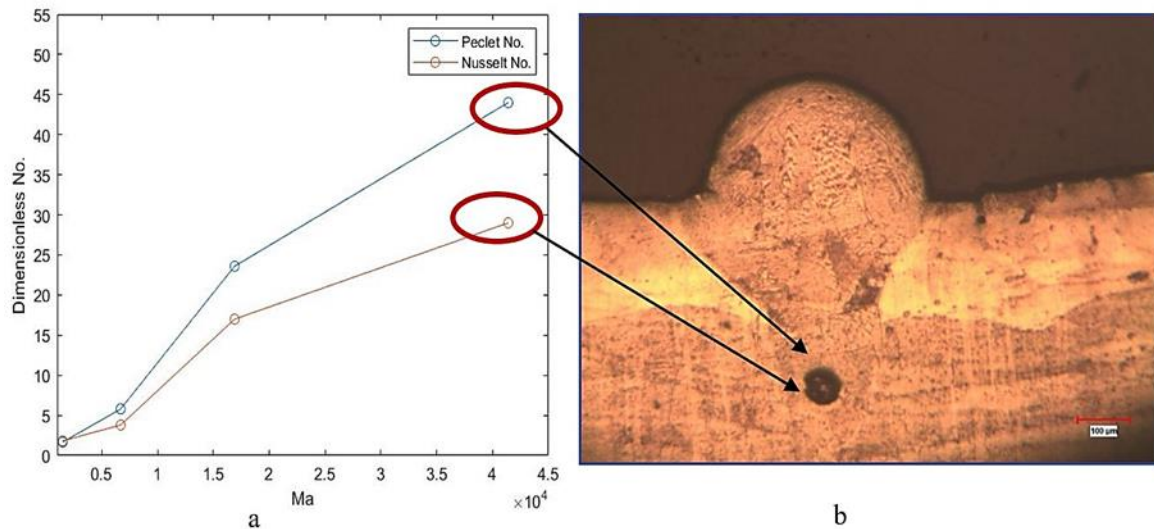
Figure 25: a) Peclet and Nusselt Number with increasing Marangoni Number for increasing laser power b) Keyhole observed in the bead at laser power and speed of 300W/200mm/s corresponding to Pe= 54, Nu=44 and Ma=41000

4.5. Discussion

This work was carried out to capture the multi-physics nature consisting of simultaneous heat transfer and fluid dynamic during the process (LPBF). An updated model based on our previous work was built including experimentally obtained thermophysical properties at elevated temperatures, laser intensity profile along the depth that follows beer lambert law, marangoni force, recoil pressure and buoyancy effect. Thermal response was captured first using energy, mass and momentum balance equation. Temperature profile is not symmetric because of the non-linear and non-gaussian nature of laser-powder bed interaction during the process. Velocity of fluid reaches its peak immediately after the

center of the beam due to higher thermal gradient around that region, prompting the fluid to accelerate towards the lower temperature point. The region before the highest temperature has a greater surface molten pool area as the laser has already scanned over that portion and temperature gradient is comparatively lower. The thermo-fluid model was able to perfectly capture the melt pool flow due to various driving forces. Fluid flows radially outwards due to the surface tension gradients and buoyancy drives the flow in the upward direction just below the center of the beam. The radial flow transfers heat from the center region to the molten pool, elongating both the length (x axis) and width (y axis) of the melt pool region [129]. Increase in laser power generally accompanies a gradual shift from conduction to keyhole type because of evaporation. Temperature exceeding the vaporization point creates recoil pressure, minimizing the highest temperature and creating a depression in the melt pool, which increases the depth of the molten region. Higher laser power generates significantly increased velocity, resulting in higher values of the dimensionless numbers like Nusselt number, Peclet number and marangoni number. These dimensionless numbers are low at lower laser powers like 100W, indicating heat is transferred away mainly through conduction from the hot region. Consequently, the melt pool size is small as there is not enough fluid movement to make a larger liquid zone that can create delamination due to lack of adhesion with the solid layer. As the power increases, melt pool starts to behave violently, making a possible transition from laminar to turbulent flow. Temperature difference inside the melt pool is low at higher marangoni number, which minimizes the contribution from thermal conduction, and most of the heat is carried out by convection. This is evident from experimental image from *Figure 25,* where the Peclet and Nusselt number are 54 and 44 respectively. The solid layers beneath

73

the powder layer go through repeated melting and solidification because of deep melt pool, which can generate considerable residual stress in those layers. The image shows a keyhole formation that incorporates pores and other defects, indicating the intense nature of the fluid motion.

4.7. Conclusion

A robust three-dimensional thermo-fluid Multiphysics models along with a 2-D model was built to analyze the thermal response and fluid flow of Inconel 718 during LPBF process. The major findings are summarized below:

- The temperature profile is lower and wider for the new model compared to the previous one owing to the updated material properties, surface tension properties and recoil pressure.

- Fluid flows on both sides of the center of the melt pool because of the high temperature gradient. The velocity is higher at the leading font of the melt pool.

- Melt pool expands in both x and y direction mainly due to violent marangoni convection inside the melt pool. Melt pool depth depend on marangoni convection, buoyancy, and recoil pressure.

- Both melt pool width and depth were validated against experimentally obtained data and improved results were observed.

- Contribution of convective heat transfer was established based on dimensionless numbers like Peclet, Nusselt and marangoni numbers. At higher power, these numbers significantly increase suggesting significant melt pool flow and subsequent convection.

CHAPTER 5

PROCESS OPTIMIZATION USING STATISTICAL ANALYSIS

This chapter discusses various features like contact angle, porosity, melt pool size, keyhole in the bead. ImageJ is used to quantify the features. Afterwards, this data is used to conduct single and multi response analysis to optimize laser power and scan speed with respect to these features.

5.1. Setup

Inconel 718 alloy, based on nickel was chosen due to its superior properties over a wide temperature range and high corrosion resistance. After the samples were built, they were polished and etched. A Nikon DS-Fi1 camera attached to a Meiji Techno optical microscope was used to take the images of the solidified beads. 8-12 images from each sample was taken for proper representation of the samples. The following table contains the laser power and scan speeds that were used during the experiments. ImageJ was used to quantify the features. As it was mostly a manual process, measurements were taken multiple times for the same sample to ensure precision.

Table ix: Process Parameters

	40W	100W	150W	200W	300W
200 mm/s	T1	T4	T10	T13	T19
700 mm/s	T2	T5	T11	T14	T20
1200 mm/s	T3	T6	T12	T15	T21
1700 mm/s		T7		T16	T22
2200 mm/s		T8		T17	T23
2500 mm/s		T9		T18	T24

5.2. Melt Pool Features

5.2.1 Contact Angle

Contact angle is the angle between the melt pool and the layer beneath it [130]. It determines the wettability of the molten powder particle with the previous layer. Proper wettability ensures there is a good adhesion between the layers. Inadequate adhesion between layers can result in warped built [80] as the surface tension forces become dominant over the adhesive forces. High contact angle ($>90^0$) can result in balling phenomenon, which distorts the material. Thus, it is desirable to have a low contact angle to ensure proper wetting and adhesion between layers. Image analysis software ImageJ was used to measure the contact angle of the experimentally obtained bead. The bead images were obtained using optical microscopy.
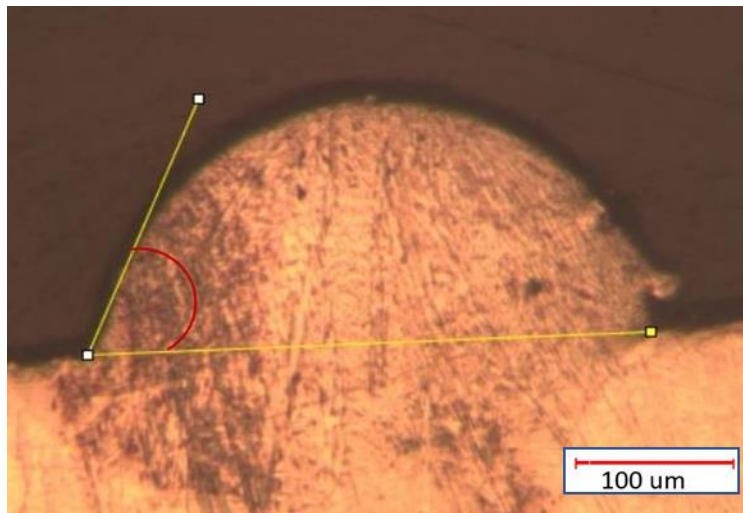
Figure 26: Contact Angle Measurement

5.2.2 Porosity

 Gas entrapped pores can have both spherical and irregular shape. They are characterized by size of around 5-30 microns for powder bed fusion (PBF) process and greater than 50 micron for direct energy deposition (DED) [131]. These defects can be attributed to the manufacturing of powders using gas atomization process that can carry some gases entrapped within the powders [132]. In addition, process parameters that create strong marangoni flow can trap some of the pores within the melt pool. Presence of porosity can have a detrimental effect on material fatigue life as well as mechanical properties. ImageJ was used to identify the porosities in the melt pool using threshold. The borderline thresholds were removed during analysis.
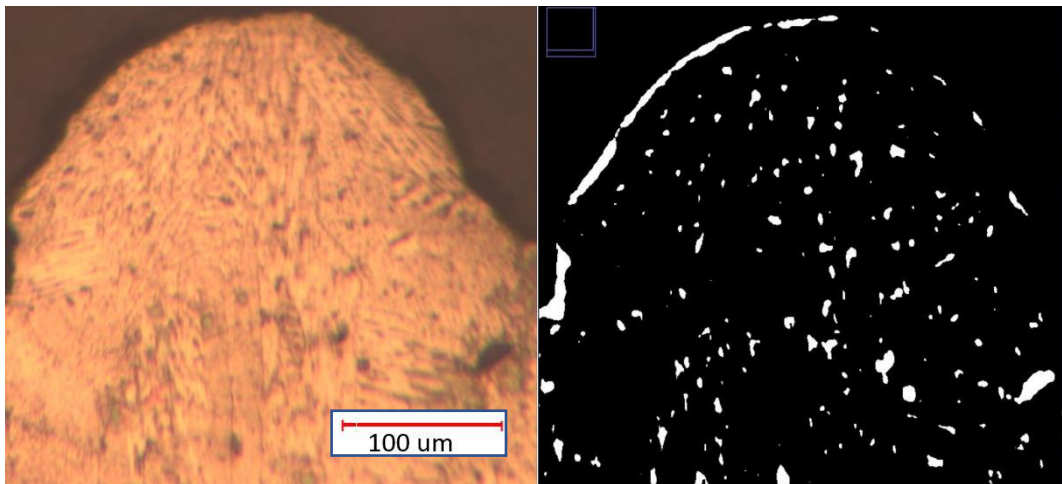
Figure 27*: Identification of porosities in melt pool

5.2.3 Keyhole and Voids

Although keyhole is more dominant in welding due to high laser power and low welding speed, it can be present during AM as well as high laser powers are being used lately in this process. High energy density on the powder material can cause evaporation, creating recoil pressure, which depresses the melt pool, creating a narrow and deep keyhole shape

[133]. Keyhole needs to be controlled, otherwise it can leave voids inside the melt pool containing vapor. Metals that have low thermal conductivity facilitate the formation of keyhole as they help accumulate enough heat to start evaporation.
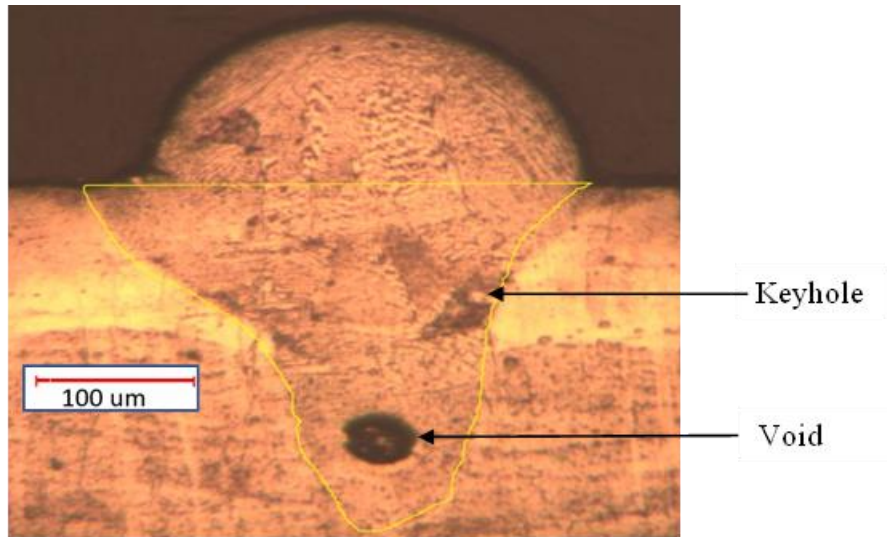
Figure 28: Voids associated with keyholes

5.2.4 Melt Pool

Melt pool is one of the most important features in additively manufactured parts. Size of the melt pool is extremely important. If the area of the melt pool is too large, then it repeatedly melts and solidifies 4-5 layers beneath the current layer, which can create residual stress in those layers. Residual stress can result in distortion of the part of the built. On the other hand, a shallow melt pool can cause inadequate adhesion with the previously solidified layer. So, choosing optimum process parameter is of paramount importance to create the standard melt pool.

5.3 Result and Discussion

5.3.1 Single Response Analysis

As part of the statistical analysis, the features were identified and quantified using ImageJ software. Analysis of variance (Anova)was used to identify if the process variables like laser power and scan speed have any significant impact on the melt pool features, or not. Anova starts with the assumption that there is no significant influence of the input variables on output, termed as null hypothesis. F- ratio or F statistic is calculated using the mean of different groups to observe if output changes significantly based on change in the input. If the value of F ratio is sufficiently large, then it can be concluded that there is a strong correlation between the input and output, and a change in the input will affect the output substantially.

$$\text{F ratio} = \frac{Mean\ of\ squares\ between\ (MS_v)}{Mean\ of\ squares\ within\ (MS_e)} \tag{38}$$

$$MS = \frac{Sum\ of\ squares\ between\ (SS)}{Degrees\ of\ freedom\ (DF)} \tag{39}$$

DF=Number of groups of a variable-1

$$Total\ sum\ of\ square, SS_t = \sum(Y_{ij} - Y_{tot.avg})^2 \tag{40}$$

$$Sum\ of\ square\ between, SS_v = \sum(Y_{i.avg} - Y_{tot.avg})^2 \tag{41}$$

$$Sum\ of\ squares\ within, SS_e = SS_t - SS_v \tag{42}$$

Here, Y_{ij} denotes the jth observation of the ith group.

Equation 38-42 provides the steps to calculate the F ratio. Here, between refers to the value of an output between the groups of a variable, and within means the value of an output within a specific group of variable. For example, when we try to find out the F ratio of contact angle in terms of laser power, sum of square between refers to the variation of mean

of contact angle between different laser powers (40W, 100W, 150W and so on) compared to the average of all the contact angles, which can be calculated using equation 41. On the other hand, sum of square within refers to the variation of contact angle within a specific group. For instance, there are multiple values contact angle for a laser power of 40W. Sum of square within calculates the variation of contact angle within this group of 40W, does the same for all the other groups such as 100,150,200,300 W, and sums it all up to get the total sum of square between as shown in equation 41. We get the mean of square by dividing the sum of square by degree of freedom. Finally, F-ratio is calculated by diving the mean of squares between by mean of squares within. So, if F-ratio is larger than the critical value of F provided in the F distribution table [134], then the variability of contact angle for different laser power is large enough to ascertain that laser power has a significant effect on contact angle. P-value is another way to determine if the null hypothesis is true. Null hypothesis states that the mean value of contact angle for different laser powers is same. p value is the probability of accepting the null hypothesis. A smaller p value indicates a small chance for the null hypothesis being true. For example, if the p value is 0.05, then there is only 5% chance that the mean contact angle value for all the laser power will be same, which is really low. Thus, we can reject the null hypothesis.

Pareto chart is another tool that demonstrates the significance of the process parameters on the response parameter. It is a bar chart that shows the relative effect of different parameters on a specific response or output parameter. It also provides a reference line at 5% significant level. The process parameters are considered significant if they exceed that reference line.

Figure 29 shows the effects of laser power and scan speed on contact angle. The values of contact angle vary between 29 degrees at 300 W/200 mm/s to 135.2 degrees at 40W/2500 mm/s. Contact angle decreases with higher laser power and lower scan speed because of the high energy input. At lower energy input, the angle is more than 90 degrees. At this level, balling phenomena occurs that can create delamination and distort the part. It can be observed from both *Figure 29* and F-value of *Table x* that both laser power and scan speed play significant role on contact angle. Anova for interaction between laser power and scan speed was not possible to conduct, as we did not have contact angle data for all combinations of laser power and scan speed, as some of the beads were broken due to balling and other defects.
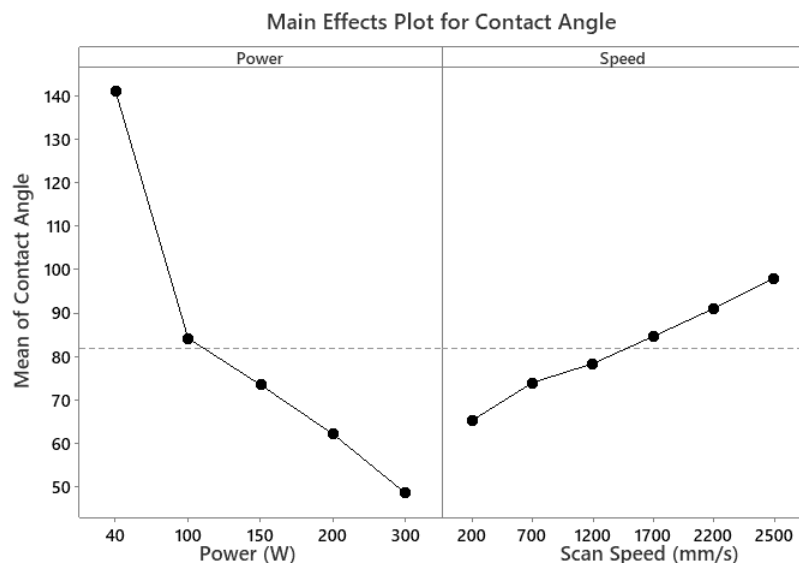
Figure 29*: Individual impact of laser power and scan speed on mean contact angle*

Table x: Analysis of Variance

Source	DF	Adj SS (Degree²)	Adj MS (Degree²)	F-Value	P-Value
Power	4	16439.6	4109.89	138.87	0.00001
Speed	5	1872.2	374.44	30.87	0.00003

Equation 43 provides the regression equation for contact angle with R^2 value of 83.2% based on the process variables. This equation is an important tool as it can be used to predict the output value for unknown values of laser power and scan speed.

$$Contact\ Angle = 111.18 - 0.2714 * Power + 0.00834 * Speed \qquad (43)$$

It can also be observed from the pareto chart in *Figure 30* that both power and speed effects are higher than the threshold detected by the 95% confidence interval (red dotted line), laser power being the most dominant influencing factor. The values in x axis denotes deviation from overall mean for each process parameter. The more the deviation, the more likely it is that the specific parameter is more influential on the output value.
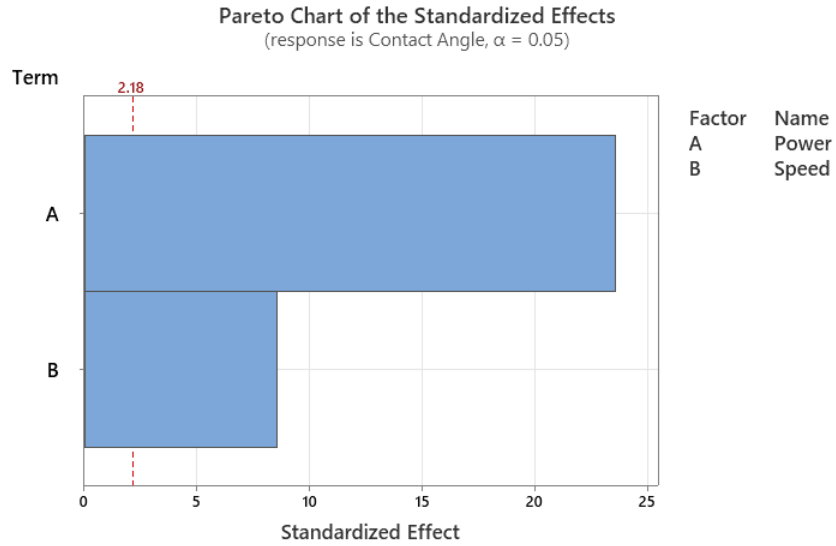
Figure 30: Pareto Chart of the Standardized Effect of Laser Power and Scan Speed on

Contact Angle

5.3.1.2. Porosity

The pores in the melt pool varied in the range of 5 to 40 microns in diameters. Due to improper melting, lack of fusion occurs at lower laser powers and higher scan speeds, resulting in higher number of pores. Although there is less porosity at higher laser powers due to proper wetting, some pores still exist due to the larger melt pool size.
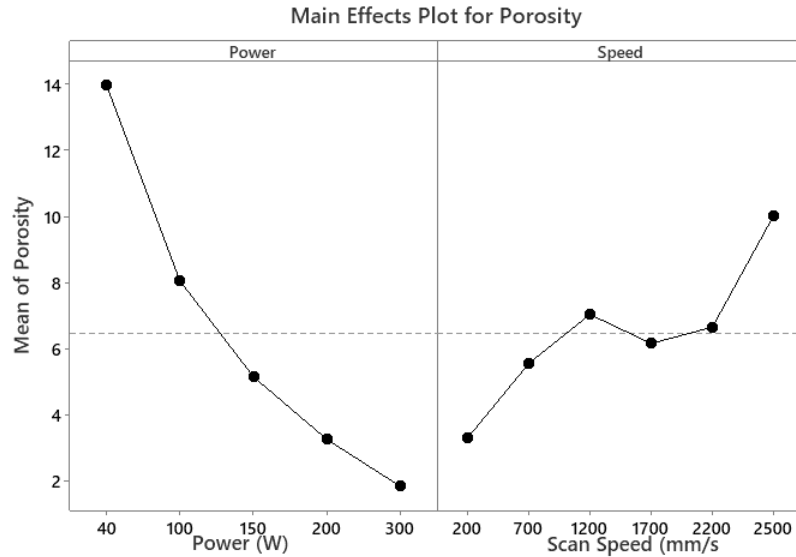
Figure 31:Individual Impact of Laser Power and Scan Speed on Mean Contact Angle

Laser power has significant impact on pore percentage, as is evident from Anova analysis and pareto chart. Although scanning speed has a much less significance, it still is above the threshold level, and hence cannot be ignored while optimize the process to minimize porosity in the melt pool.

Table xi: Analysis of Variance

Source	DF	Adj SS	Adj MS	F-Value	P-Value
Power	4	321.06	80.266	22.52	0.000
Speed	5	68.04	13.607	5.82	0.027
Error	12	42.76	3.564		

The regression analysis detected a R^2 value of 77.6%. This is due to the fact that, although porosity varied in a fairly consistent manner with laser power, it was somewhat scattered for scanning speed.

$$Porosity = 10.75 - 0.04046 * Power + 0.001550 * Speed \qquad (44)$$
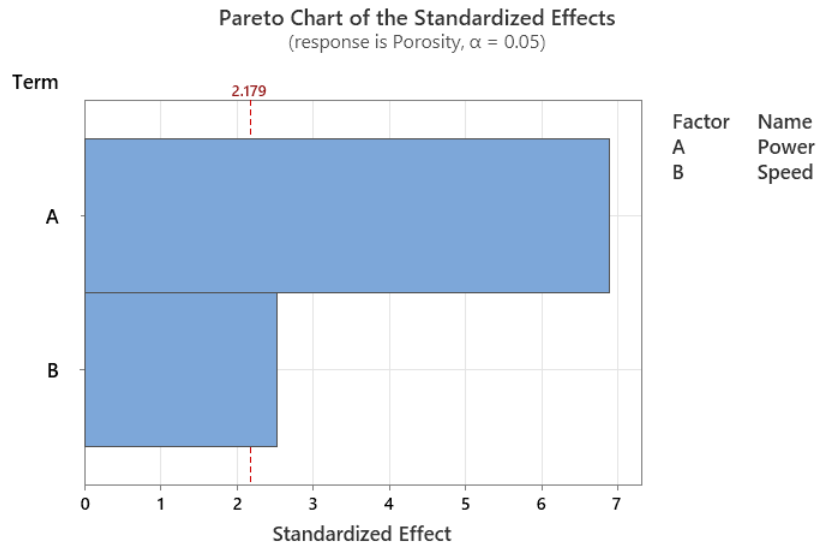
Figure 32: Pareto chart of the standardized effect of laser power and scan speed on

porosity

5.3.1.3 Melt Pool

Power and speed have similar, but opposite effect on melt pool size. Melt pool size can be extremely small and shallow for lower energy input, while high energy can create large enough molten pool that melts 5-6 layers of previously solidified layers. Anova analysis show that p value for power and speed is 0.007 and 0.010, indicating significant effect on melt pool area.
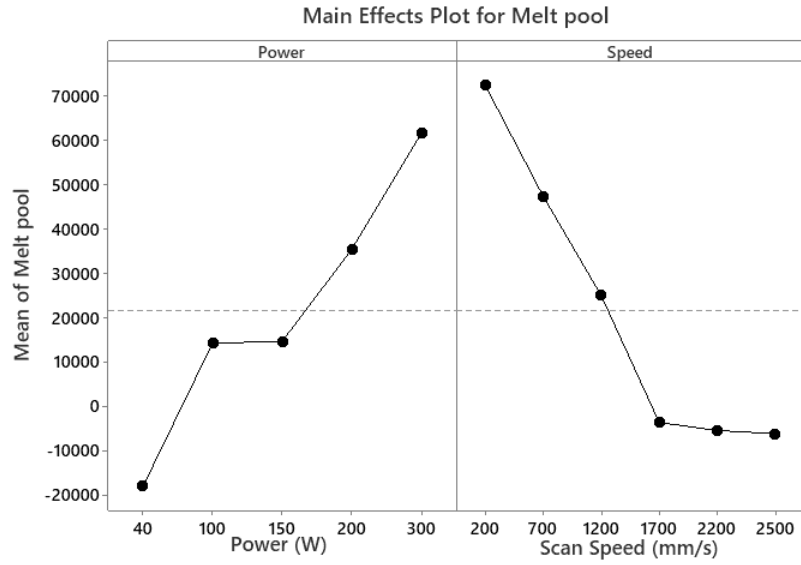
Figure 33: Individual Impact of Laser Power and Scan Speed on Mean Contact Angle

Table xii: Analysis of Variance

Source	DF	Adj SS (μm^4)	Adj MS (μm^4)	F-Value	P-Value
Power	4	13541394444	3385348611	5.95	0.007
Speed	5	14474970343	2894994069	5.49	0.010
Error	12	6826062381	568838532		

R^2 value from regression analysis was 74.4%.

$$Melt\ Pool = 27865 + 270.1 * Power - 33.45 * Speed \qquad (45)$$
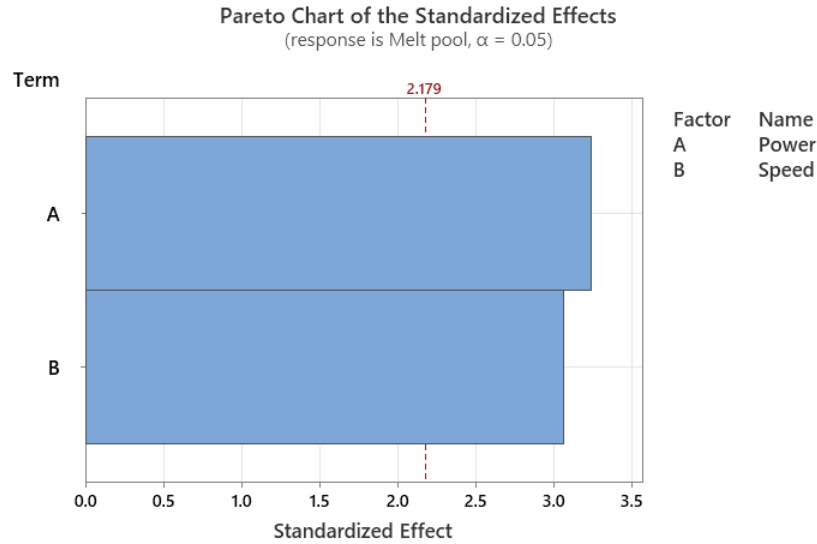
Figure 34: Pareto Chart of the Standardized Effect of Laser Power and Scan Speed on

Melt Pool

5.3.1.4. Keyhole and Void

keyholes were found only in 3 sets of beads: 300 W laser power with scan speeds of 200

and 700 mm/s, 200 W laser power with 200 mm/s scan speed due to high energy input.

The size of the keyhole was 18036 square microns on average. Diameter of the voids within

the keyholes due to gas entrapment was around 81 microns on average.

5.3.2. Multi Response Analysis and Optimization

To observe the combined effect of both the process parameters on the all the outputs or

responses simultaneously. Response optimizer was used in minitab. Response optimization

enables to identify the optimum values of the variables to achieve the desired set of output

values.

Table xiii shows the optimization parameters for each output. Target for contact angle was

set as 50 degrees. As lower contact angle can produce higher surface roughness [83], a

lower limit of 30 was chosen. On the other hand, a higher angle of contact with the substrate can facilitate balling formation, which is why an upper bound of 80 degrees was selected. As, porosity is not desirable in additively manufactured parts, minimum value was set as the target value. For melt pool area, a range was chosen which ensures proper adhesion with the previous layer as well as makes sure that repeated solidification and melting is prevented to avoid residual stress. Keyhole area and void were avoided during multi response analysis as we did not have enough data for these features.

Table xiii: Parameters Set for Response Optimization

Response	Goal	Lower	Target	Upper	Weight	Importance
Contact Angle (Degrees)	Target	30	50.0	80	1	1
Porosity (%)	Minimum		1.0	4	1	1
Melt pool (μm^2)	Target	30000	50000	70000	1	1

After examining all the combinations of input, 150 W laser power and 200 mm/s scan speed (*Table xiv*) was selected as the optimum values of process parameters to provide the desired output target values. Minitab uses the regression equation and parameter settings to calculate the best fits. The standard error of the fit (SE fit) estimates the variation in the estimated mean response for the specified variable settings. The smaller the standard error, the more precise the predicted mean response [135]. Standard error long with the fit can be used to calculate the confidence interval for the responses. a 95% confidence interval was

calculated based on 1.96 standard errors above and below the predicted mean. The SE fit

for all the responses are provided in *Table xiv*, along with confidence interval.

Table xiv: Multiple Response Prediction

Power (W)	150	0.7647		
Speed (mm/s)	200			
Response		Fit	SE Fit	95% CI
Contact Angle (Degrees)		**56.82**	3.44	(50.07, 63.56)
Porosity (%)		**2.01**	0.87	(0.3048, 3.71)
Melt pool (μm^2)		**55424**	6578	(42531,68316)

One of the most important parameters in multi response analysis is composite desirability, which is shown in the table. For multiple response parameters, it is difficult to get all the optimum response parameters for a single combination of process inputs. For this reason, Minitab maximizes the composite desirability. The composite desirability combines the individual desirability of all the response variables into a single measure. Individual desirability for target response is defined as [136]:

$$d_i = (\frac{Y_i - L_i}{T_i - L_i})^{r_i} \tag{46}$$

$$d_i = (\frac{U_i - Y_i}{U_i - T_i})^{r_i} \tag{47}$$

Here, Y is the predicted value, L is the lowest acceptable value, U is the highest acceptable value, T is the target value and r is the importance of the ith response. Composite desirability is defined as:

$$D = (d_1 \times d_2 \times d_3 \times \dots d_n)^{\frac{1}{n}} \tag{48}$$

Here, n is the number of response or outputs.

For example, it can be observed that the composite desirability of 150W/200 mm/s combination of laser power and scan speed is 0.7647. This combination of power and speed has produced the values of response optimizer (Fit column in **Table xiv**) that are closest to the target values compared to other combinations of process parameters. So, the composite desirability of other combinations of laser power and scan speed are less than 0.7647. Based on this composite desirability values, 150W of laser power and 200 mm/s of scan speed was chosen as the optimum process parameter, that is the closest to the target value set by the user.

5.4. Conclusion:

- This work discusses about the different features of a melt pool, i.e: contact angle, porosity, melt pool size, keyhole area and void.

- ImageJ was used to measure and quantify the size of the features. The measured values were plotted against laser power and scan speed. Contact angle and porosity decrease with increasing laser power and decreasing scanning speed, while the process parameters had the opposite effect on melt pool size.

- Single response statistical analysis was conducted to assess the impact of process variables. Both the process parameters have significant impact on the measured responses, laser power being the most dominant factor between them.

- Multi response analysis was performed to optimize the process using minitab Laser power of 150 W and scan speed of 200 mm/s was found to have produced melt pool with the most desired features.

91

CHAPTER 6

CONTRIBUTIONS TO THE SCIENTIFIC COMMUNITY

This research focused on several aspects of laser metal AM that can improve the understanding of the process significantly. The important findings of this work that can benefit the scientific community are listed in the following points:

- The multi-physics simulation model was developed using a non-Gaussian process, which produced a better result of thermal history and bead geometry than conventional Gaussian process when compared against experimental results. The imitation of simulation results with experimental data has been long sought by the scientific community. This demonstration can pave the way of improved modeling effort in understanding the AM process in a more comprehensive way.

- There was a lack of experimental data of thermo-physical properties of metallic from the bulk of literature, which is of utmost importance to construct a robust computational model of additive process. This work not only presents the experimental results of thermal conductivity, diffusivity and heat capacity at elevated temperatures, but also compares them with available analytical models, which will be helpful for other materials as well. Regression analysis was also conducted for thermal conductivity at higher temperatures. This work is expected to be immensely helpful to the computational modeling community.

- Statistical analysis conducted in this thesis to optimize the process parameters will significantly benefit the additive society. Quantification of the features like contact angle, porosity, melt pool area etc. along the melt pool region based on laser power and scan speed, and combining them together to perform a single as well as multi response

analysis is rare in literature. The scientific community will get an idea how these features change with changing process variables, and they can choose what process parameters will fit their purpose based on this quantitative as well as qualitative analysis.

CHAPTER 7

CONCLUSION AND FUTURE WORK

This research fundamentally provides the development of laser powder bed fusion process (LPBF) through a combination of computational, experimental, analytical, and statistical modeling. The 1st chapter discusses about the interaction between laser and powder particles using energy, mass and momentum balance equation to build a 3D model. The temperature profile and the melt pool obtained using the 3D model is used to simulate the solidified bead shape through level set method. The simulation results are compared and validated against experimental values. Elemental evaporation of the alloying elements was also calculated analytically as well as experimentally to observe the concentration change of the elements during the process.

While working on the 1st project, the researchers realized the lack of experimentally obtained thermophysical properties of metallic powders at elevated temperature, which is of paramount importance to build a computationally robust model. To bridge this gap, thermal diffusivity, conductivity and heat capacity of the 5 common metallic powders that are used in AM process were tested at temperatures up to 1400 degrees Celsius. Primary finding was that the thermophysical properties behave in a non-monotonic nature at lower temperatures, but start increasing due to sintering as the temperature increases. The results were compared against literature values that are generally used because of the lack in literature. A regression analysis for thermal conductivity was conducted at higher temperature. These results, along with several other modifications (Including marangoni effect and recoil pressure directly in the energy equation), were used in the computational model. The temperature profile and bead geometry result significantly improved after the

modifications. The nature of the melt pool flow due to marangoni flow and buoyancy were discussed. The fluid moves away from the center of the melt pool towards lower temperature region owing to marangoni convection on both sides, carrying the heat away in the process. A thorough dimensional analysis using peclet number, Nusselt number and marangoni number was conducted to analyze the impact of convective and conductive heat flow during the process. It was observed that convective flow was the main source of heat transport within the melt pool for all laser power and scan speed combinations, and more pronounced at higher energy inputs.

As part of the last project, statistical analysis was conducted for several features in the melt pool: i.e. contact angle, porosity, melt pool size etc. ImageJ was used to quantify the features. Full factorial Anova and regression analysis was performed on these values to optimize the process. A multi response analysis was also conducted to find the optimum laser power and scan speed to get the desired values of these features. 150 W laser power and 200 mm/s scan speed was determined to be the process parameters that produce features closest to the target values.

In summary, this thesis was performed to understand the complex heat transfer and fluid flow phenomena that occur in powder bed fusion AM process. Computational modeling, experimental work and statistical analysis was done to build a comprehensive and robust model to present a full picture of the process as well as optimize the process in terms of laser power and scan speed.

The research initiated in this study provides further motivation to the following topics:

- This research was conducted in laminar flow regime. Turbulent flow model can be applied to do a comprehensive analysis for high laser energy input, which can

reflect the true nature of keyhole produced due to the higher laser power. Different types of techniques, such as L-VEL, algebraic yPlus, Spalart-Allmaras, k-ε, k-ω, low Reynolds number k-ε, SST, and v2-f turbulence models can be tested to analyze the nature of the melt pool flow at turbulent regime.

- The statistical analysis was conducted along the melt X-Y cross section. A more detailed analysis can be performed by analyzing the top surface of the build and using this data in combination with the melt pool data to perform a comprehensive multi- response analysis.

- Artificial intelligence is in the forefront of research and technology in modern world. Machine learning techniques have been introduced in AM sector as well. A predictive Convolutional Neural Network (CNN) algorithm can be built that can predict the laser power and scan speed from the images of melt pool as a part of process optimization that can make process optimization more convenient by reducing computational cost.

REFERENCES

[1]   L. Ladani, J. Romano, W. Brindley, and S. Burlatsky, "Effective liquid conductivity for improved simulation of thermal transport in laser beam melting powder bed technology," *Addit. Manuf.*, vol. 14, pp. 13–23, 2017, doi: 10.1016/j.addma.2016.12.004.

[2]   F. Ahsan, J. Razmi, and L. Ladani, "Multi-Physics Modeling of Laser Interaction With Surface in Powder Bed Melting Process," *Vol. 2 Adv. Manuf.*, no. November, p. V002T02A085, 2018, doi: 10.1115/IMECE2018-86566.

[3]   J. Romano, L. Ladani, and M. Sadowski, "Thermal Modeling of Laser Based Additive Manufacturing Processes within Common Materials," *Procedia Manuf.*, vol. 1, 2015, doi: 10.1016/j.promfg.2015.09.012.

[4]   R. Andreotta, L. Ladani, and W. Brindley, "Finite element simulation of laser additive melting and solidification of Inconel 718 with experimentally tested thermal properties," *Finite Elem. Anal. Des.*, vol. 135, no. July, pp. 36–43, 2017, doi: 10.1016/j.finel.2017.07.002.

[5]   M. Sadowski, L. Ladani, W. Brindley, and J. Romano, "Optimizing quality of additively manufactured Inconel 718 using powder bed laser melting process," *Addit. Manuf.*, vol. 11, pp. 60–70, 2016, doi: 10.1016/j.addma.2016.03.006.

[6]   S. A. Khairallah, A. T. Anderson, A. Rubenchik, and W. E. King, "Acta Materialia Laser powder-bed fusion additive manufacturing : Physics of complex melt fl ow and formation mechanisms of pores , spatter , and denudation zones," *Acta Mater.*, vol. 108, pp. 36–45, 2016, doi: 10.1016/j.actamat.2016.02.014.

[7]   F. Lopez, P. Witherell, and B. Lane, "Identifying Uncertainty in Laser Powder Bed Fusion Additive Manufacturing Models," *J. Mech. Des.*, vol. 138, no. 11, Nov. 2016, doi: 10.1115/1.4034103.

[8]   D. D. Gu, W. Meiners, K. Wissenbach, and R. Poprawe, "Laser additive manufacturing of metallic components: materials, processes and mechanisms," *https://doi.org/10.1179/1743280411Y.0000000014*, vol. 57, no. 3, pp. 133–164, May 2013, doi: 10.1179/1743280411Y.0000000014.

[9]   Z. Xiang, M. Yin, Z. Deng, X. Mei, and G. Yin, "Simulation of Forming Process of Powder Bed for Additive Manufacturing," *J. Manuf. Sci. Eng.*, vol. 138, no. 8, Aug. 2016, doi: 10.1115/1.4032970.

[10]   L. Ladani and F. Ahsan, "Laser Interaction with Surface in Powder Bed Melting Process and Its Impact on Temperature Profile, Bead and Melt Pool Geometry," in *Minerals, Metals and Materials Series*, 2019, pp. 319–329, doi: 10.1007/978-3-030-05861-6_29.

[11]   "Six Core Advantages of Additive Manufacturing | Jabil."
        https://www.jabil.com/blog/advantages-of-additive-manufacturing.html (accessed
        Aug. 31, 2021).

[12]   "What is Additive Manufacturing technology and it's types."
        https://engineeringproductdesign.com/knowledge-base/additive-manufacturing-
        processes/ (accessed Sep. 23, 2021).

[13]   D. D. Gu, W. Meiners, K. Wissenbach, and R. Poprawe, "Laser additive
        manufacturing of metallic components: Materials, processes and mechanisms," *Int.
        Mater. Rev.*, vol. 57, no. 3, pp. 133–164, 2012, doi:
        10.1179/1743280411Y.0000000014.

[14]   J. P. Kruth, G. Levy, F. Klocke, and T. H. C. Childs, "Consolidation phenomena in
        laser and powder-bed based layered manufacturing," *CIRP Ann. - Manuf.
        Technol.*, vol. 56, no. 2, pp. 730–759, 2007, doi: 10.1016/j.cirp.2007.10.004.

[15]   F. Verhaeghe, T. Craeghs, J. Heulens, and L. Pandelaers, "A pragmatic model for
        selective laser melting with evaporation," *Acta Mater.*, vol. 57, no. 20, pp. 6006–
        6012, 2009, doi: 10.1016/j.actamat.2009.08.027.

[16]   "The Powder Bed Fusion process | Prima Additive."
        https://www.primaadditive.com/the-powder-bed-fusion-process/ (accessed Aug.
        31, 2021).

[17]   "How process parameters drive successful metal AM part production."
        https://www.metal-am.com/articles/70927-
        2/?__cf_chl_managed_tk__=pmd_NFoGNEmnyDUpY6prafB3yvcTu7L32jo3klZ
        yN6cW3cQ-1630680841-0-gqNtZGzNAvujcnBszQjR (accessed Sep. 03, 2021).

[18]   "Towards optimal processing of additive manufactured metals for high strain rate
        properties - Google Search."
        https://www.google.com/search?q=Towards+optimal+processing+of+additive+ma
        nufactured+metals+for+high+strain+rate+properties&rlz=1C1CHBF_enUS919US
        919&sxsrf=AOaemvLIwQY1mdwSiuLWUC_y8XCd-
        f1LXQ%3A1630684056431&ei=mEMyYfzrGY_d-
        gTL8LWoBA&oq=Towards+optimal+processing+of+additive+manufactured+met
        als+for+high+strain+rate+properties&gs_lcp=Cgdnd3Mtd2l6EAMyBAgjECcyBA
        gAEB5KBAhBGABQkB1YkB1gqB9oAHACeACAAWqIAWqSAQMwLjGYAQ
        CgAQHAAQE&sclient=gws-wiz&ved=0ahUKEwj8l7K_k-
        PyAhWPrp4KHUt4DUUQ4dUDCA4&uact=5 (accessed Sep. 03, 2021).

[19]   I. A. Roberts, C. J. Wang, R. Esterlein, M. Stanford, and D. J. Mynors,
        "International Journal of Machine Tools & Manufacture A three-dimensional finite
        element analysis of the temperature field during laser melting of metal powders in
        additive layer manufacturing," *Int. J. Mach. Tools Manuf.*, vol. 49, no. 12–13, pp.
        916–923, 2009, doi: 10.1016/j.ijmachtools.2009.07.004.

[20] L. Dong, A. Makradi, S. Ahzi, and Y. Remond, "Three-dimensional transient finite element analysis of the selective laser sintering process," vol. 9, pp. 700–706, 2008, doi: 10.1016/j.jmatprotec.2008.02.040.

[21] P. Michaleris, "Modeling metal deposition in heat transfer analyses of additive manufacturing processes," *Finite Elem. Anal. Des.*, vol. 86, pp. 51–60, 2014, doi: 10.1016/j.finel.2014.04.003.

[22] Y. S. Lee and W. Zhang, "Modeling of heat transfer , fluid flow and solidification microstructure of nickel-base superalloy fabricated by laser powder bed fusion," *Addit. Manuf.*, vol. 12, pp. 178–188, 2016, doi: 10.1016/j.addma.2016.05.003.

[23] I. Kovaleva, O. Kovalev, and I. Smurov, "Model of Heat and Mass Transfer in Random Packing Layer of Powder Particles in Selective Laser Melting," *Phys. Procedia*, vol. 56, no. C, pp. 400–410, Jan. 2014, doi: 10.1016/J.PHPRO.2014.08.143.

[24] "On thermal modeling of Additive Manufacturing processes | Elsevier Enhanced Reader." https://reader.elsevier.com/reader/sd/pii/S1755581717300494?token=F3CA93818 5BD1BD045D1E69C7B8601864C186F9DAA533084F026BD27CE67215149E4 D3621118EC54E785C420206BD395&originRegion=us-east-1&originCreation=20210901175709 (accessed Sep. 01, 2021).

[25] M. R. Yavari, K. D. Cole, and P. Rao, "Thermal Modeling in Metal Additive Manufacturing Using Graph Theory," *J. Manuf. Sci. Eng.*, vol. 141, no. 7, Jul. 2019, doi: 10.1115/1.4043648.

[26] J. Horak *et al.*, "power continuous wave laser perforation of thin metal plates Numerical modeling and characterization of the laser – matter interaction during high-power continuous wave laser perforation of thin metal plates," vol. 28003, no. 2015, 2017.

[27] M. V. Deo and P. Michaleris, "Mitigation of welding induced buckling distortion using transient thermal tensioning," *http://dx.doi.org/10.1179/136217103225008919*, vol. 8, no. 1, pp. 49–54, Feb. 2013, doi: 10.1179/136217103225008919.

[28] J. Ning, W. Wang, X. Ning, D. E. Sievers, H. Garmestani, and S. Y. Liang, "Analytical Thermal Modeling of Powder Bed Metal Additive Manufacturing Considering Powder Size Variation and Packing," *Mater. 2020, Vol. 13, Page 1988*, vol. 13, no. 8, p. 1988, Apr. 2020, doi: 10.3390/MA13081988.

[29] R. Jendrzejewski, G. Śliwiński, M. Krawczuk, and W. Ostachowicz, "Temperature and stress fields induced during laser cladding," *Comput. Struct.*, vol. 82, no. 7–8, pp. 653–658, Mar. 2004, doi: 10.1016/J.COMPSTRUC.2003.11.005.

[30] K. Dai and L. Shaw, "Distortion minimization of laser-processed components through control of laser scanning patterns," *Rapid Prototyp. J.*, vol. 8, no. 5, pp. 270–276, Dec. 2002, doi: 10.1108/13552540210451732.

[31] F. Ahsan and L. Ladani, "Temperature Profile, Bead Geometry, and Elemental Evaporation in Laser Powder Bed Fusion Additive Manufacturing Process," *Jom*, vol. 72, no. 1, pp. 429–439, 2020, doi: 10.1007/s11837-019-03872-3.

[32] D. Zhang, P. Zhang, Z. Liu, Z. Feng, C. Wang, and Y. Guo, "Thermofluid field of molten pool and its effects during selective laser melting (SLM) of Inconel 718 alloy," *Addit. Manuf.*, vol. 21, pp. 567–578, May 2018, doi: 10.1016/j.addma.2018.03.031.

[33] M. Bayat, V. K. Nadimpalli, S. Mohanty, and J. H. Hattel, "Resolving the effects of local convective heat transfer via adjustment of thermo-physical properties in pure heat conduction simulation of Laser Powder Bed Fusion (L-PBF)," *IOP Conf. Ser. Mater. Sci. Eng.*, vol. 861, no. 1, 2020, doi: 10.1088/1757-899X/861/1/012006.

[34] Y. Chen *et al.*, "In-situ Synchrotron imaging of keyhole mode multi-layer laser powder bed fusion additive manufacturing," *Appl. Mater. Today*, vol. 20, p. 100650, Sep. 2020, doi: 10.1016/j.apmt.2020.100650.

[35] A. Raghavan, H. L. Wei, T. A. Palmer, and T. Debroy, "Heat transfer and fluid flow in additive manufacturing," no. August, 2013, doi: 10.2351/1.4817788.

[36] A. Foroozmehr, M. Badrossamay, and E. Foroozmehr, "Finite Element Simulation of Selective Laser Melting process considering Optical Penetration Depth of laser in powder bed," *JMADE*, vol. 89, pp. 255–263, 2016, doi: 10.1016/j.matdes.2015.10.002.

[37] F. Process, "Finite Element Analysis of Interaction of Laser Beam with Material in Laser Metal Powder Bed Fusion Process," 2018, doi: 10.3390/ma11050765.

[38] D. S. Nagesh and G. L. Datta, "Prediction of weld bead geometry and penetration in shielded metal-arc welding using artificial neural networks," vol. 123, pp. 303–312, 2002.

[39] C. H. Fu and Y. B. Guo, "3-DIMENSIONAL FINITE ELEMENT MODELING OF SELECTIVE LASER MELTING TI-6AL-4V ALLOY."

[40] V. Manvatkar, A. De, and T. Debroy, "Heat transfer and material flow during laser assisted multi-layer additive manufacturing," *J. Appl. Phys.*, vol. 116, no. 12, 2014, doi: 10.1063/1.4896751.

[41] A. International, "F3055 − 14a, ASTM: Standard Specification for Additive Manufacturing Nickel Alloy (UNS N07718) with Powder Bed Fusion," *F3055 -*

14a, no. March, pp. 1–8, 2014, doi: 10.1520/F3055-14A.Copyright.

[42] T. Mukherjee, J. S. Zuback, A. De, and T. DebRoy, "Printability of alloys for additive manufacturing," *Sci. Rep.*, vol. 6, pp. 1–8, 2016, doi: 10.1038/srep19717.

[43] P. A. A. Khan and T. Debroy, "Alloying element vaporization and weld pool temperature during laser welding of AlSl 202 stainless steel," *Metall. Trans. B*, vol. 15, no. 4, pp. 641–644, 1984, doi: 10.1007/BF02657284.

[44] T. Liu, L. J. Yang, H. L. Wei, W. C. Qiu, and T. Debroy, "Composition change of stainless steels during keyhole mode laser welding," *Weld. J.*, vol. 96, no. 7, pp. 258s-270s, 2017.

[45] Z. Malekshahi Beiranvand, F. Malek Ghaini, H. Naffakh Moosavy, M. Sheikhi, M. J. Torkamany, and M. Moradi, "The relation between magnesium evaporation and laser absorption and weld penetration in pulsed laser welding of aluminum alloys: Experimental and numerical investigations," *Opt. Laser Technol.*, vol. 128, p. 106170, Aug. 2020, doi: 10.1016/J.OPTLASTEC.2020.106170.

[46] C. T. Hsu, P. Cheng, and K. W. Wong, "Modified Zehner-Schlunder models for stagnant thermal conductivity of porous media," *Int. J. Heat Mass Transf.*, vol. 37, no. 17, pp. 2751–2759, 1994, doi: 10.1016/0017-9310(94)90392-1.

[47] T. H. C. Childs, M. Berzins, G. R. Ryder, and A. Tontowi, "Selective laser sintering of an amorphous polymer - Simulations and experiments," *Proc. Inst. Mech. Eng. Part B J. Eng. Manuf.*, vol. 213, no. 4, pp. 333–349, 1999, doi: 10.1243/0954405991516822.

[48] S. SUMIN SIH and J. W. BARLOW, "The Prediction of the Emissivity and Thermal Conductivity of Powder Beds," *Part. Sci. Technol.*, vol. 22, no. 3, pp. 291–304, Jul. 2004, doi: 10.1080/02726350490501682a.

[49] A. V. Gusarov, T. Laoui, L. Froyen, and V. I. Titov, "Contact thermal conductivity of a powder bed in selective laser sintering," *Int. J. Heat Mass Transf.*, vol. 46, no. 6, pp. 1103–1109, 2003, doi: 10.1016/S0017-9310(02)00370-8.

[50] G. R. Hadley, "Thermal conductivity of packed metal powders," *Int. J. Heat Mass Transf.*, vol. 29, no. 6, pp. 909–920, Jun. 1986, doi: 10.1016/0017-9310(86)90186-9.

[51] J. S. Agapiou and M. F. DeVries, "An experimental determination of the thermal conductivity of a 304l stainless steel powder metallurgy material," *J. Heat Transfer*, vol. 111, no. 2, pp. 281–286, 1989, doi: 10.1115/1.3250675.

[52] S. Zhang, B. Lane, J. Whiting, and K. Chou, "An Investigation into Metallic Powder Thermal Conductivity in Laser Powder-Bed Fusion Additive Manufacturing," pp. 1796–1807, 2018.

[53]   M. Andisheh-Tadbir, E. Kjeang, and M. Bahrami, "Thermal conductivity of microporous layers: Analytical modeling and experimental validation," *J. Power Sources*, vol. 296, pp. 344–351, Aug. 2015, doi: 10.1016/j.jpowsour.2015.07.054.

[54]   Z. Ling, J. Chen, T. Xu, X. Fang, X. Gao, and Z. Zhang, "Thermal conductivity of an organic phase change material/expanded graphite composite across the phase change temperature range and a novel thermal conductivity model," *Energy Convers. Manag.*, vol. 102, pp. 202–208, Jul. 2015, doi: 10.1016/j.enconman.2014.11.040.

[55]   W. W. M. Siu and S. K. Lee, "Effective conductivity computation of a packed bed using constriction resistance and contact angle effects," *Int. J. Heat Mass Transf.*, vol. 43, no. 21, pp. 3917–3924, 2000, doi: 10.1016/S0017-9310(00)00051-X.

[56]   Y. Asakuma, I. Honda, and T. Yamamoto, "Numerical approach to predicting the effective thermal conductivity of a packed bed of binary particles," *Powder Technol.*, vol. 354, pp. 886–892, Sep. 2019, doi: 10.1016/j.powtec.2019.07.023.

[57]   S. Ayatollahi, N. Saber, M. J. Amani, and A. Bitaab, "Mathematical investigation of effective thermal conductivity in fractured porous media," *J. Porous Media*, vol. 9, no. 7, pp. 625–635, 2006, doi: 10.1615/JPorMedia.v9.i7.20.

[58]   K. Boomsma and D. Poulikakos, "On the effective thermal conductivity of a three-dimensionally structured fluid-saturated metal foam," *Int. J. Heat Mass Transf.*, vol. 44, no. 4, pp. 827–836, Feb. 2001, doi: 10.1016/S0017-9310(00)00123-X.

[59]   R. Singh, R. S. Bhoopal, and S. Kumar, "Prediction of effective thermal conductivity of moist porous materials using artificial neural network approach," *Build. Environ.*, vol. 46, no. 12, pp. 2603–2608, 2011, doi: 10.1016/j.buildenv.2011.06.019.

[60]   M. R. Alkahari, T. Furumoto, T. Ueda, A. Hosokawa, R. Tanaka, and M. S. Abdul Aziz, "Thermal conductivity of metal powder and consolidated material fabricated via selective laser melting," *Key Eng. Mater.*, vol. 523–524, no. March, pp. 244–249, 2012, doi: 10.4028/www.scientific.net/KEM.523-524.244.

[61]   G. R. Langecker and R. Rautenbach, "A method for measuring the thermal conductivity of isotropically compressed powders," *Powder Technol.*, vol. 15, no. 1, pp. 39–42, Sep. 1976, doi: 10.1016/0032-5910(76)80028-9.

[62]   S. Ramdas, A. Chowdhury, and A. Lakshminarayana, "IMPACT OF ACCELERATED THERMAL AGING ON THERMOMECHANICAL PROPERTIES OF OIL-IMMERSED FR-4 PRINTED CIRCUIT BOARDS," *researchgate.net*, 2019, Accessed: Sep. 07, 2021. [Online]. Available: https://www.researchgate.net/profile/Shrinath-Ramdas/publication/336533723_Impact_of_Accelerated_Thermal_Aging_on_Thermo-Mechanical_Properties_of_Oil-Immersed_FR-

4_Printed_Circuit_Boards/links/5e5073c7a6fdcc2f8f5533b2/Impact-of-Accelerated-Thermal-Aging-on-Thermo-Mechanical-Properties-of-Oil-Immersed-FR-4-Printed-Circuit-Boards.pdf.

[63]   A. S. M. R. Chowdhury *et al.*, "A Comparative Study of Thermal Aging Effect on the Properties of Silicone-Based and Silicone-Free Thermal Gap Filler Materials," *Mater. 2021, Vol. 14, Page 3565*, vol. 14, no. 13, p. 3565, Jun. 2021, doi: 10.3390/MA14133565.

[64]   S. Ramdas, A. S. M. R. R. Chowdhury, A. Lakshminarayana, R. Bhandari, A. Misrak, and D. Agonafer, "Impact of Thermal Aging on Thermomechanical Properties of Oil-Immersed Printed Circuit Boards," *SMTA Int.*, pp. 772–778, 2019.

[65]   M. Kabir *et al.*, "ENHANCING THE RELIABILITY OF 3D PACKAGE BY ANALYZING CRACK BEHAVIOR ON TSV THROUGH STRUCTURAL OPTIMIZATION AND COMPARING MATERIAL PROPERTIES OF THE PACKAGE The University of Texas at Arlington," *SMTA Int.*, pp. 56–65, 2020.

[66]   T. Chauhan, R. Bhandari, K. B. Sivaraju, A. S. M. R. Chowdhury, and D. Agonafer, "Impact of Immersion Cooling on Thermomechanical Properties of Low-Loss Material Printed Circuit Boards," *J. Enhanc. Heat Transf.*, vol. 28, no. 7, pp. 73–90, 2021, doi: 10.1615/jenhheattransf.2021039486.

[67]   M. P. Hossain and K. Paul, "Thermal conductivity analysis of single-walled carbon nanotube using finite element modeling," *AIP Conf. Proc.*, vol. 1980, Jul. 2018, doi: 10.1063/1.5044375.

[68]   D. A. G. Bruggeman, "Berechnung verschiedener physikalischer Konstanten von heterogenen Substanzen. I. Dielektrizitätskonstanten und Leitfähigkeiten der Mischkörper aus isotropen Substanzen," *Ann. Phys.*, vol. 416, no. 7, pp. 636–664, Jan. 1935, doi: 10.1002/ANDP.19354160705.

[69]   N. Zamel, J. Becker, and A. Wiegmann, "Estimating the thermal conductivity and diffusion coefficient of the microporous layer of polymer electrolyte membrane fuel cells," *J. Power Sources*, vol. 207, pp. 70–80, Jun. 2012, doi: 10.1016/J.JPOWSOUR.2012.02.003.

[70]   G. Abbas Gohar, T. Manzoor, and A. N. Shah, "Investigation of thermal and mechanical properties of Cu-Al alloys with silver addition prepared by powder metallurgy," *J. Alloys Compd.*, vol. 735, pp. 802–812, Feb. 2018, doi: 10.1016/J.JALLCOM.2017.11.176.

[71]   S. Manikandan, S. Ramanathan, and V. Ramakrishnan, "A calorimetric study of Ti-6Al-4V alloy," *Indian J. Sci. Technol.*, vol. 6, no. 4, pp. 4262–4267, 2013.

[72]   "The heat capacity of inconel 718 from 313 to 1053 K - PDF Free Download." .

[73] M. F. Zäh and S. Lutzmann, "Modelling and simulation of electron beam melting," *Prod. Eng.*, vol. 4, no. 1, pp. 15–23, Feb. 2010, doi: 10.1007/s11740-009-0197-6.

[74] Z. Wang and M. Liu, "Dimensionless analysis on selective laser melting to predict porosity and track morphology," *J. Mater. Process. Technol.*, vol. 273, p. 116238, Nov. 2019, doi: 10.1016/j.jmatprotec.2019.05.019.

[75] B. Rankouhi, A. K. Agrawal, F. E. Pfefferkorn, and D. J. Thoma, "A dimensionless number for predicting universal processing parameter boundaries in metal powder bed additive manufacturing," *Manuf. Lett.*, vol. 27, pp. 13–17, Jan. 2021, doi: 10.1016/j.mfglet.2020.12.002.

[76] T. Mukherjee, V. Manvatkar, A. De, and T. DebRoy, "Dimensionless numbers in additive manufacturing," *J. Appl. Phys.*, vol. 121, no. 6, 2017, doi: 10.1063/1.4976006.

[77] M. S. Rahman, P. J. Schilling, P. D. Herrington, and U. K. Chakravarty, "A Comparison of the Thermo-Fluid Properties of Ti-6Al-4V Melt Pools Formed by Laser and Electron-Beam Powder-Bed Fusion Processes," *J. Eng. Mater. Technol.*, vol. 143, no. 2, pp. 1–13, 2021, doi: 10.1115/1.4048371.

[78] F. Ahsan, J. Razmi, and L. Ladani, "Experimental measurement of thermal diffusivity, conductivity and specific heat capacity of metallic powders at room and high temperatures," *Powder Technol.*, vol. 374, pp. 648–657, 2020, doi: 10.1016/j.powtec.2020.07.043.

[79] B. Dikshit, G. R. Zende, M. S. Bhatia, and B. M. Suri, "Convection in molten pool created by a concentrated energy flux on a solid metal target," *Phys. Fluids*, vol. 21, no. 8, 2009, doi: 10.1063/1.3210763.

[80] M. Fateri, S. Pitikaris, and M. Sperl, "Investigation on Wetting and Melting Behavior of Lunar Regolith Simulant for Additive Manufacturing Application," *Microgravity Sci. Technol.*, vol. 31, no. 2, pp. 161–167, 2019, doi: 10.1007/s12217-019-9674-5.

[81] Y. Yuan and T. R. Lee, "Contact angle and wetting properties," *Springer Ser. Surf. Sci.*, vol. 51, no. 1, pp. 3–34, 2013, doi: 10.1007/978-3-642-34243-1_1.

[82] J. C. Haley, J. M. Schoenung, and E. J. Lavernia, "Modelling particle impact on the melt pool and wettability effects in laser directed energy deposition additive manufacturing," *Mater. Sci. Eng. A*, vol. 761, no. May, p. 138052, 2019, doi: 10.1016/j.msea.2019.138052.

[83] D. Triantafyllidis, L. Li, and F. H. Stott, "The effects of laser-induced modification of surface roughness of Al2O3-based ceramics on fluid contact angle," *Mater. Sci. Eng. A*, vol. 390, no. 1–2, pp. 271–277, 2005, doi: 10.1016/j.msea.2004.08.016.

[84] M. Brennan, J. S. Keist, and T. A. Palmer, "Defects in Metal Additive Manufacturing Processes," *Addit. Manuf. Process.*, vol. 24, pp. 277–286, 2020, doi: 10.31399/asm.hb.v24.a0006557.

[85] Y. Murakami, H. Masuo, Y. Tanaka, and M. Nakatani, "Defect Analysis for Additively Manufactured Materials in Fatigue from the Viewpoint of Quality Control and Statistics of Extremes," *Procedia Struct. Integr.*, vol. 19, pp. 113–122, 2019, doi: 10.1016/j.prostr.2019.12.014.

[86] N. Sanaei, A. Fatemi, and N. Phan, "Defect characteristics and analysis of their variability in metal L-PBF additive manufacturing," *Mater. Des.*, vol. 182, p. 108091, 2019, doi: 10.1016/j.matdes.2019.108091.

[87] G. Tapia, A. H. Elwany, and H. Sang, "Prediction of porosity in metal-based additive manufacturing using spatial Gaussian process models," *Addit. Manuf.*, vol. 12, pp. 282–290, 2016, doi: 10.1016/j.addma.2016.05.009.

[88] O. Kwon, H. G. Kim, W. Kim, G. H. Kim, and K. Kim, "A convolutional neural network for prediction of laser power using melt-pool images in laser powder bed fusion," *IEEE Access*, vol. 8, pp. 23255–23263, 2020, doi: 10.1109/ACCESS.2020.2970026.

[89] F. Caiazzo and A. Caggiano, "Laser direct metal deposition of 2024 al alloy: Trace geometry prediction via machine learning," *Materials (Basel).*, vol. 11, no. 3, 2018, doi: 10.3390/ma11030444.

[90] K. Paul and L. Ladani, "Relationship between peak density and acoustic scattering in high-frequency ultrasound wave propagation," *SN Appl. Sci.*, vol. 2, no. 8, pp. 1–12, 2020, doi: 10.1007/s42452-020-03208-w.

[91] S. K. Rauniyar and K. Chou, "Melt Pool Analysis and Mesoscale Simulation of Laser Powder Bed Fusion Process (L-PBF) with Ti-6Al-4V Powder Particles," *JOM*, vol. 71, no. 3, pp. 938–945, Mar. 2019, doi: 10.1007/s11837-018-3208-2.

[92] "W.-B. Li, H. Engstro¨m, J. Powell, Z. Tan, and C. Magnusson, Lasers Eng. 5, 175–183 ~1996!."

[93] "acuracy of gaussian beam.pdf." .

[94] D. R. Tobergte *et al.*, "Gaussian beam optics," *Science (80-.).*, vol. 5, no. 9, p. aae0330, 2010, doi: 10.1126/science.aae0330.

[95] "'Lasers and laser-related equipment – Test methods for laser beam widths, divergence angles and beam propagation ratios' (2005)." .

[96] "What Is the Marangoni Effect?" https://www.comsol.com/multiphysics/marangoni-effect (accessed Mar. 03, 2021).

[97] "Two-Phase Flow Modeling Guidelines - 1239 - Knowledge Base." .

[98] "Recommended Values of Thermophysical Properties for Selected Commercial Alloys - 1st Edition." https://www.elsevier.com/books/recommended-values-of-thermophysical-properties-for-selected-commercial-alloys/mills/978-1-85573-569-9 (accessed Mar. 03, 2021).

[99] K. C. Mills, Y. M. Youssef, Z. Li, and Y. Su, "Calculation of Thermophysical Properties of Ni-based Superalloys," *ISIJ Int.*, vol. 46, no. 5, pp. 623–632, 2006, doi: 10.2355/ISIJINTERNATIONAL.46.623.

[100] Y. S. Lee, P. Nandwana, and W. Zhang, "Dynamic simulation of powder packing structure for powder bed additive manufacturing," *Int. J. Adv. Manuf. Technol. 2018 961*, vol. 96, no. 1, pp. 1507–1520, Feb. 2018, doi: 10.1007/S00170-018-1697-3.

[101] T. Debroy and S. A. David, "Physical processes in fusion welding," *Rev. Mod. Phys.*, vol. 67, no. 1, pp. 85–112, 1995, doi: 10.1103/RevModPhys.67.85.

[102] C. B. Alcock, "Vapor Pressure Equations for the Metallic Elements," pp. 5–7, 2000.

[103] B. Cheng, J. Lydon, K. Cooper, V. Cole, P. Northrop, and K. Chou, "Infrared thermal imaging for melt pool analysis in SLM: a feasibility investigation," *Virtual Phys. Prototyp.*, vol. 13, no. 1, pp. 8–13, Jan. 2018, doi: 10.1080/17452759.2017.1392685.

[104] S. Yagi and D. Kunii, "Studies on effective thermal conductivities in packed beds," *AIChE J.*, vol. 3, no. 3, pp. 373–381, 1957, doi: 10.1002/aic.690030317.

[105] G. Bugeda, M. Cervera, and G. Lombera, "Numerical prediction of temperature and density distributions in selective laser sintering processes," *Rapid Prototyp. J.*, vol. 5, no. 1, pp. 21–26, 1999, doi: 10.1108/13552549910251846.

[106] J. FRANCL and W. D. KINGERY, "Thermal Conductivity: IX, Experimental Investigation of Effect of Porosity on Thermal Conductivity," *J. Am. Ceram. Soc.*, vol. 37, no. 2, pp. 99–107, Feb. 1954, doi: 10.1111/j.1551-2916.1954.tb20108.x.

[107] "DSC 25 – TA Instruments." .

[108] "Thermal Diffusivity - an overview | ScienceDirect Topics." .

[109] "DXF 900 – TA Instruments." .

[110] W. J. Parker, R. J. Jenkins, C. P. Butler, and G. L. Abbott, "Flash method of determining thermal diffusivity, heat capacity, and thermal conductivity," *J. Appl. Phys.*, vol. 32, no. 9, pp. 1679–1684, 1961, doi: 10.1063/1.1728417.

[111] J. Romano, L. Ladani, J. Razmi, and M. Sadowski, "Temperature distribution and melt geometry in laser and electron-beam melting processes - A comparison among common materials," *Addit. Manuf.*, vol. 8, pp. 1–11, 2015, doi: 10.1016/j.addma.2015.07.003.

[112] Y. Zhang and A. Faghri, "Melting and resolidification of a subcooled mixed powder be with moving gaussian heat source," *J. Heat Transfer*, vol. 120, no. 4, pp. 883–891, 1998, doi: 10.1115/1.2825907.

[113] "Stainless Steel ALLOY 304/304L – UNS S30400 / S304033 | Penn Stainless Products." .

[114] "316 Stainless Steel Sheet, Coil & Bar - AMS 5524, AMS 5507 - 316L S Stainless Supplier." .

[115] C. S. Kim, *75-55.* .

[116] T. Slezak, J. Zmywaczyk, and P. Koniorczyk, "Thermal diffusivity investigations of the titanium grade 1 in wide temperature range," *AIP Conf. Proc.*, vol. 2170, no. November, 2019, doi: 10.1063/1.5132738.

[117] "Thermal Diffusivity | Electronics Cooling." https://www.electronics-cooling.com/2007/08/thermal-diffusivity/ (accessed Nov. 04, 2021).

[118] رازی .ز. ا. م, "No Title1384," الحاوی جلد بیستم.

[119] "No Titleالبترول."

[120] R. W. Powell, R. P. Tye, and M. J. Hickman, "The thermal conductivity of nickel," *Int. J. Heat Mass Transf.*, vol. 8, no. 5, pp. 679–688, 1965, doi: 10.1016/0017-9310(65)90017-7.

[121] J.-M. Oh, K.-H. Heo, W.-B. Kim, G.-S. Choi, and J.-W. Lim, "Sintering Properties of Ti-6Al-4V Alloys Prepared Using Ti/TiH 2 Powders," 2012, doi: 10.2320/matertrans.M2012304.

[122] D. S. Smith *et al.*, "Thermal conductivity of porous materials," *J. Mater. Res.*, vol. 28, no. 17, pp. 2260–2272, 2013, doi: 10.1557/jmr.2013.179.

[123] "Nonisothermal Flow." https://www.comsol.com/multiphysics/nonisothermal-flow (accessed Mar. 03, 2021).

[124] U. Roy and P. K. Roy, "Advances in heat intensification techniques in shell and tube heat exchanger," in *Advanced Analytic and Control Techniques for Thermal Systems with Heat Exchangers*, Elsevier, 2020, pp. 197–207.

[125] E. Bender, "Numerical heat transfer and fluid flow. VonS. V. Patankar.

Hemisphere Publishing Corporation, Washington - New York - London. McGraw Hill Book Company, New York 1980. 1. Aufl., 197 S., 76 Abb., geb., DM 71,90," *Chemie Ing. Tech.*, vol. 53, no. 3, pp. 225–225, Jan. 1981, doi: 10.1002/cite.330530323.

[126] L. M. Flows and W. Phenom-, "Eötvös number," pp. 1–2, 2011.

[127] J. Y. Lee, S. H. Ko, D. F. Farson, and C. D. Yoo, "Mechanism of keyhole formation and stability in stationary laser welding," *J. Phys. D. Appl. Phys.*, vol. 35, no. 13, pp. 1570–1576, Jul. 2002, doi: 10.1088/0022-3727/35/13/320.

[128] E. Repper, "Defect formation in laser welded steels after use of corrosion protection coating," 2017.

[129] H. Shen, J. Yan, and X. Niu, "Thermo-Fluid-Dynamic Modeling of the Melt Pool during Selective Laser Melting for AZ91D Magnesium Alloy," *Materials (Basel).*, vol. 13, no. 18, p. 4157, Sep. 2020, doi: 10.3390/ma13184157.

[130] R. Li, J. Liu, Y. Shi, L. Wang, and W. Jiang, "Balling behavior of stainless steel and nickel powder during selective laser melting process," *Int. J. Adv. Manuf. Technol.*, vol. 59, no. 9–12, pp. 1025–1035, 2012, doi: 10.1007/s00170-011-3566-1.

[131] S. K. Everton, M. Hirsch, P. I. Stavroulakis, R. K. Leach, and A. T. Clare, "Review of in-situ process monitoring and in-situ metrology for metal additive manufacturing," *Mater. Des.*, vol. 95, pp. 431–445, 2016, doi: 10.1016/j.matdes.2016.01.099.

[132] F. H. Kim and S. P. Moylan, "Literature Review of Metal Additive Manufacturing Defects,US Department of Commerce, National Institute of Standards and Technology.," *National*, pp. 1–17, 2018, [Online]. Available: http://nvlpubs.nist.gov/nistpubs/ams/NIST.AMS.100-16.pdf.

[133] W. E. King *et al.*, "Observation of keyhole-mode laser melting in laser powder-bed fusion additive manufacturing," *J. Mater. Process. Technol.*, vol. 214, no. 12, pp. 2915–2925, 2014, doi: 10.1016/j.jmatprotec.2014.06.005.

[134] "F-Distribution Tables." http://www.socr.ucla.edu/Applets.dir/F_Table.html (accessed Oct. 07, 2021).

[135] "All statistics and graphs for Response Optimizer."

[136] "What are individual desirability and composite desirability?"